# Charles University Faculty of Mathematics and Physics

# HABILITATION DISSERTATION



# Crystals for Modern Science and Applications

RNDr. Klára Uhlířová, Ph.D.

Department of Condensed Matter Physics

December 2024

#### **Preface**

This work presents a summary of my main scientific interest in condensed matter physics since my PhD studies, which I have devoted to experimental studies of electronic properties of a relatively wide spectrum of material. As suggested in the title of this thesis, a significant part of my contribution lies in crystal growth; however, I should not forget to mention that I also focus on several characterization and measurement techniques. My career as a crystal grower started with my PhD studies at the Department of Condensed Matter Physics. From my supervisor, Vladimír Sechovský, I got a special opportunity. The opportunity was called an empty laboratory space with one resistive furnace, and the task was to implement the molten metal flux growth method for the preparation of new materials. To get some practical experience, I first visited the group of Gerard Venturini at the University Henri Poincaré, Nancy and then spent eight weeks at Ames laboratory in the group of Paul Canfield. There, I could see how world-class quality single crystals can be grown in a relatively modestly equipped laboratory, but most importantly, I could see the philosophy of focusing on popper materials, which would advance my knowledge in physics and material research. That significantly increased my motivation to follow trends in physics and materials science and look for challenges that crystal growth offers. This approach has persisted until the present time.

The only period in my career where I was not growing crystals was during my postdoctoral research at Leiden University in the group of Jan Aarts, where I worked on a collaborative project focused on graphene research in the years 2011 - 2013. To a great extent, my decision not to prepare my samples had both bright and dark sides. It allowed me to focus more on other experimental techniques, such as lithography, charge transport studies, or scanning probe microscopy techniques, but it limited my access to suitable samples and information about the sample preparation history. Consequently, I made the decision not to be only dependent on samples from external sources in the future.

After my postdoc in Leiden, I returned to Prague in 2013. In about the first five years after returning, I partially focused on heavy fermion physics, which I had already studied during my PhD and then continued by mentoring and collaborating with, at that time a PhD student, Marie Kratochvílová. Together, we grew several members of a new series of new heavy fermion superconductors, mainly Ce<sub>3</sub>PdIn<sub>11</sub> and Ce<sub>3</sub>PtIn<sub>11</sub>. Having in mind problems with the separation of phase pure Ce<sub>2</sub>PdIn<sub>8</sub> single crystals, together with experience with electron-beam lithography from Leiden, I decided to employ the Focused Ion Beam technique to fabricate tiny phase-pure samples for resistivity measurements. At the time, it was the rather unexplored approach for which I obtained a postdoctoral grant. Together with my bachelor student Jiří Volný, we spent almost two years of trials, connected with regular travels around Prague labs, because each step required some equipment we did not have in our laboratory. After the help

of Philip Moll, who kindly shared with us one important step he invented, we had the method working.

My second field of interest was initiated by a short collaboration on studies of polycrystalline CuMnAs with X. Martí from the Department of Spintronics and Nanoelectronics Institute of Physics of the Czech Academy of Sciences. Later, it developed in gradually increasing collaboration with and other members of the group such as Karel Výborný, with whom I work on studies of magnetic anisotropy in selected antiferromagnets and with Helena Reichlová and Dominik Kriegner, with whom I have currently discussed further studies of the so-called altermagnetic materials into two-dimensional systems, which is currently one of the hottest topics of spintronics.

My inclination toward two-dimensional materials is motivated by another project that I have been working on for the last three years. That project is studies of misfit layered compounds, where we discovered moiré sliding ferroelectricity, a completely new phenomenon in two-dimensional van der Waals materials, which has been of high experimental interest in about the last three years.

This thesis is divided into four main chapters and a summary. The first three chapters present my contribution to studies of heavy fermion superconductors, antiferromagnetic spintronics, and sliding ferroelectricity in misfit layered compounds. The last chapter presents the necessary effort to obtain high-quality samples for all the research. In the summary, I discuss the achievements and future perspectives of my research.

# Contents

1 Sı	•	yered Heavy Fermion Materials - A Crossover between Magnetism and and an analysis of the second seco	and 6
51	1.1	Heavy fermion materials, superconductivity	
	1.2	The layered $Ce_nT_mIn_{3n+2m}$ system	
	1.3	Summary	
2	Ma	terials for antiferromagnetic spintronics	. 12
	2.1	Antiferromagnetic Spintronics	12
	2.2	CuMnAs	. 13
	2.2	Exploring the (Cu-Mn) <sub>2</sub> As line of the Cu-Mn-As diagram	15
	2.3	NaMnAs	16
	2.4	MnTe – the first experimentally confirmed altermagnet	. 19
	2.5	Summary	20
3	Mi	sfit layered compounds as candidates for sliding ferroelectricity	21
	3.1	Ferroelectricity in van der Waals materials	21
	3.2	Discovery of sliding ferroelectricity in MLCs	. 22
	3.2	.1 Misfit-layered compounds	. 22
	3.2	.2 Sliding Ferroelectricity in (PbS) <sub>1.11</sub> VS <sub>2</sub>	. 23
	3.3	Summary	. 29
4	Saı	mples, the essence of materials research	. 30
	4.1	The route to quality single crystals	. 30
	4.2	Microfabrication, a way to overcome sample limitations	. 38
	4.3	Summary	42
5		neral Summary	
Li	ist of c	original papers	44
D	ofonon		17

# 1 Layered Heavy Fermion Materials - A Crossover between Magnetism and Superconductivity

# 1.1 Heavy fermion materials, superconductivity

Heavy fermion materials belong to the group of strongly correlated electron systems, where the formed quasiparticles have a very high effective mass (i.e. they appear as heavy) ) [1–5] This phenomenon was first observed in 1975 in CeAl<sub>3</sub> [6] by measuring a surprisingly high specific heat coefficient, the Sommerfeld coefficient  $y = 1620 \text{ mJ mol}^{-1} \text{ K}^{-2}$ , three orders of magnitude higher than in the usual materials. The coefficient  $\gamma$ , a material constant used in an electronic specific heat, is proportional to the (thermal) effective mass; therefore, the term 'heavy fermion' is used in the cases of its high values. The formation of heavy quasiparticles is connected with a strong correlation between magnetic moments and conduction electrons in materials containing magnetic atoms. In 1979, superconductivity was discovered in CeCu<sub>2</sub>Si<sub>2</sub> [7], a material for which the BCS theory could not be applied. CeCu<sub>2</sub>Si<sub>2</sub> was then followed by many other materials such as UBe<sub>13</sub> [8,9] or UPt<sub>3</sub> [10,11] containing 4f or 5f elements summarised in several review articles [4,12–15]. At first sight, the most striking difference compared to the 'BSC superconductors' was the presence of magnetic elements in the crystal lattice. However, there have been more peculiarities in the behaviour of the new type of superconductors; a long journey full of discoveries of exotic materials and phenomena has started. The Cooper pairs can create an anisotropic p-wave spin-triplet, d-wave spin-singlet, or even f-wave spin-triplet state (so the opposite exchange symmetry of the Cooper pair wave function is preserved). This unconventional symmetry is then reflected in a strong anisotropy with characteristic nodes in the superconducting gap [14,16,17]. The character of the Fermi surface, magnetic anisotropy, or symmetry of the superconducting gap are essential input parameters for theoretical models. While conventional (s-wave) superconductors are mediated by phonon interaction, unconventional superconductivity is thought to occur in the presence of magnetic excitations or even with a coexistence with magnetic order [12,14,15,18]. When the magnetic ordering is reduced to zero by an external parameter, such as pressure, doping, or magnetic field, a continuous phase transition known as the quantum critical point (QCP) is created. It has been observed in many different systems (cuprates, pnictides, heavy fermion, and organic SC) that the highest superconducting transition temperatures, in a certain temperature-doping or temperature-pressure phase diagram, occur when the material also shows the *T*-linear behaviour, i.e., the non-Fermi liquid state [12,19,20].

# 1.2 The layered $Ce_nT_mIn_{3n+2m}$ system

An important group of heavy fermion materials, the so-called '1-1-5' and '2-1-8' tetragonal compounds were discovered in the early 2000s. Compounds are formed from CeIn<sub>3</sub> layers altered by TIn<sub>2</sub> layers (RE = Ce, T = transition metal) [21,22].

The main building block of the series, cubic **CeIn<sub>3</sub>**, is an ambient pressure antiferromagnet with a Néel temperature of 10.2 K and Fermi liquid behaviour [23]. Antiferromagnetism vanishes under a hydrostatic pressure of 2.5 GPa, being in the superconducting dome of 2.2 - 2.8 GPa with a maximum  $T_c$  of 200 mK [24,25].

A prominent role plays  $CeCoIn_5$ , an ambient pressure superconductor with the highest  $T_c$  (2.3 K) within Ce-based compounds [26]. STM [27,28] or point contact [29] showed that the superconducting gap symmetry is  $d_{x2-y2}$ . The non-Fermi liquid behaviour of the resistivity above the critical temperature indicates the vicinity of QCP [26]. The compound has an interesting H-T phase diagram with a magnetically ordered phase, called the Q-phase, between 10 and 11.4 T and temperatures below 300 mK [30,31]. The quasi-two-dimensional Fermi surface with high effective electron mass was shown by de Haas van Alphen (dHvA) experiments [32,33].

**CeRhIn**<sub>5</sub> shows fermi-liquid behaviour with antiferromagnetic transition blow  $T_N = 3.8$  K [34,35] at ambient pressure. With applied pressure, antiferromagnetism is gradually suppressed, superconductivity is induced, and  $T_c$  increases with pressure. Antiferromagnetism vanishes when  $T_N = T_c$  [21,22,36].

In CeIrIn<sub>5</sub>, the onset of superconductivity measured by resistivity ( $T_{c1} = 0.75$  K) is somewhat higher than the bulk value determined from specific heat measurements  $T_{c2} = 0.4$  K [26,37]. It is ascribed to the presence of stacking faults that create percolating superconducting slabs that lead to zero resistance above the onset of bulk superconductivity.

Ce<sub>2</sub>CoIn<sub>8</sub> and Ce<sub>2</sub>RhIn<sub>8</sub> mostly mimic the properties of their 1-1-5 counterparts, only their magnetic or superconducting transition temperatures are somewhat lower [38–42]. Ce<sub>2</sub>IrIn<sub>8</sub> shows field-induced non-Fermi liquid behaviour and random spin freezing below 0.6 K; no superconductivity was detected down to 50 mK [43–45].

Due to the layered character of the compounds, the 1-1-5s and 2-1-8s are often discussed in the context of the dimensionality of the fermi surfaces. Compared to three-dimensional CeIn<sub>3</sub>, quasi-two-dimensional (cylindrical) Fermi surfaces were measured by dHvA experiments in the 1-1-5 and 2-1-8 systems, 1-1-5s are closer to the ideal 2D Fermi surface than 2-1-8s [33,46–49]. The reason for the cylindrical Fermi surfaces is the hybridisation of d electrons of the T atom with 5p electrons from indium. This reduces the density of states near the Fermi level; there are almost no conduction electrons in the TIn<sub>2</sub> layer. Hence, looking at the crystal structure, the dimensionality is given by the stacking of layers, as depicted in Figure 1. Correlations between dimensionality, magnetism, and superconductivity can be observed, in agreement with theory, showing that reduced dimensionality leads to an increase in the critical temperature  $T_c$  [50–52].

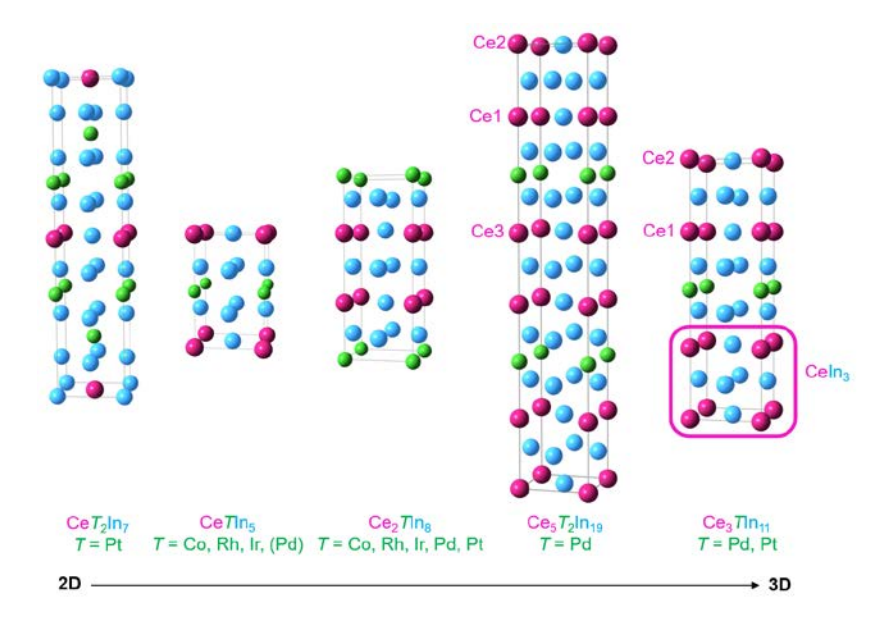


Figure 1: Crystal structure of the layered  $Ce_nT_mIn_{3n+2m}$  compounds with increasing n/m ratio. Below each structure are the transition metal elements of the existing compounds.

The 'dimensionality row' was significantly extended after new compounds with T = Pd and Pt were discovered: Ce<sub>2</sub>PdIn<sub>8</sub> [53–58][A1,A2], Ce<sub>3</sub>PdIn<sub>11</sub> [59] [A3,A4], Ce<sub>5</sub>PdIn<sub>19</sub> [59], CePt<sub>2</sub>In<sub>7</sub> [60–62], Ce<sub>2</sub>PtIn<sub>8</sub> [A3,A5] and Ce<sub>3</sub>PtIn<sub>11</sub>. As presented in Figure 1, these compounds generate smooth lines of compounds where the magnetism and superconductivity, as well as the phenomena of quantum criticality can be studied with respect to the Ce-layer separation.

Our work focused on studies of the T = Pd and Pt, and we were the first to succeed in growing phase-pure single crystals of Ce<sub>2</sub>PdIn<sub>8</sub>, Ce<sub>3</sub>PdIn<sub>11</sub> [A4] Ce<sub>3</sub>PtIn<sub>11</sub> and for the first time reported the existence and isolated single crystals of Ce<sub>2</sub>PtIn<sub>8</sub> [A3]. On looking at both series, the existence of 1-1-5 compounds with Pt and Pd has not been reported. The issues with crystal growth are discussed in [A1-A3]. From the 2-1-8 series, the Ce<sub>2</sub>PdIn<sub>8</sub> and Ce<sub>2</sub>PtIn<sub>8</sub> have been studied. The first study on polycrystalline Ce<sub>2</sub>PdIn<sub>8</sub> showed non-Fermi liquid behaviour down to 0.35 K, suggesting that the compound is in the vicinity of the quantum critical point [54]. Immediately after the reported results on polycrystals, single-crystal studies appeared to be in contradiction to the results on polycrystalline samples [55]. As described in [A1,A2], Ce<sub>2</sub>PdIn<sub>8</sub> single crystalline layers cover a CeIn<sub>3</sub> phase hidden in the core of the sample, which was a source of the antiferromagnetic signal at 10 K, leading to misinterpretation of the data [63]. We have shown that Ce<sub>2</sub>PdIn<sub>8</sub> is a heavy fermion superconductor with a critical temperature below 0.7-0.5 K that is sample dependent and suggested procedure for the preparation of Ce<sub>2</sub>PdIn<sub>8</sub> single crystals [A2]. At almost the same time, another study on polycrystalline samples (annealed 700 ° C compared to 600 ° C applied before [54,64]) showed the presence of superconductivity below 0.7 K and non-Fermi liquid behaviour above Tc, contributing to the consensus that Ce<sub>2</sub>PdIn<sub>8</sub> is a heavy fermion superconductor. Further studies closely linked Ce<sub>2</sub>PdIn<sub>8</sub> with the properties of CeCoIn<sub>5</sub>. Ce<sub>2</sub>PdIn<sub>8</sub> manifests field-induced QCP near  $H_{c2} \sim 2.3$ T [65], decrease of effective masses determined from dHvA experiments [66] or line nodes in the superconducting gap [65,67]. Only the anisotropy is lower because of the crystal structure.

Ce<sub>2</sub>PtIn<sub>8</sub> compound is paramagnetic to 50 mK. It does not show any significant field dependence of the effective masses determined from dHvA frequencies and is not considered to be in the vicinity of QCP [68] together with difficult syntheses it makes the compound less studied.

A different case, already from the point of view of crystallography, is  $Ce_3PdIn_{11}$  and  $Ce_3PdIn_{11}$  with a new type of stacking [59,69]. As shown in Figure 1, there are two distinct Ce sites in the lattice. The layers containing the Ce(1) site are surrounded on one side by the  $TIn_2$  layer and on the other side by the CeIn<sub>3</sub> layer similar to the Ce ions in  $Ce_2Tin_8$  (4mm symmetry), while the C(2) site layers are surrounded by  $CeIn_3$  layers from both sides similar to Ce ions  $CeIn_3$  (4/mmm symmetry). Both compounds also have exceptional physical properties. We have shown that  $Ce_3PdIn_{11}$  orders antiferomagnetically below  $T_1 = 1.67$  K with an order-to-order transition at  $T_N = 1.53$  K. The superconducting state is formed below  $T_c = 0.42$  K. The detailed analysis of the entropy change suggests that the magnetic moments are reduced by Kondo screening [A4] and that Ce(1) and Ce(2) sublattices are expected to have different Kondo temperatures and different RKKY interactions giving rise to complex ground state. The large value of  $(d\mu_0H_0/dT)_{T_c}$  indicates that the Cooper pairs are formed by heavy quasiparticles. The fact that superconductivity coexists with the antiferromagnetic order at ambient pressure makes the compound attractive for further studies. However, there has been a slightly better candidate with similar properties,  $Ce_3PtIn_{11}$ .

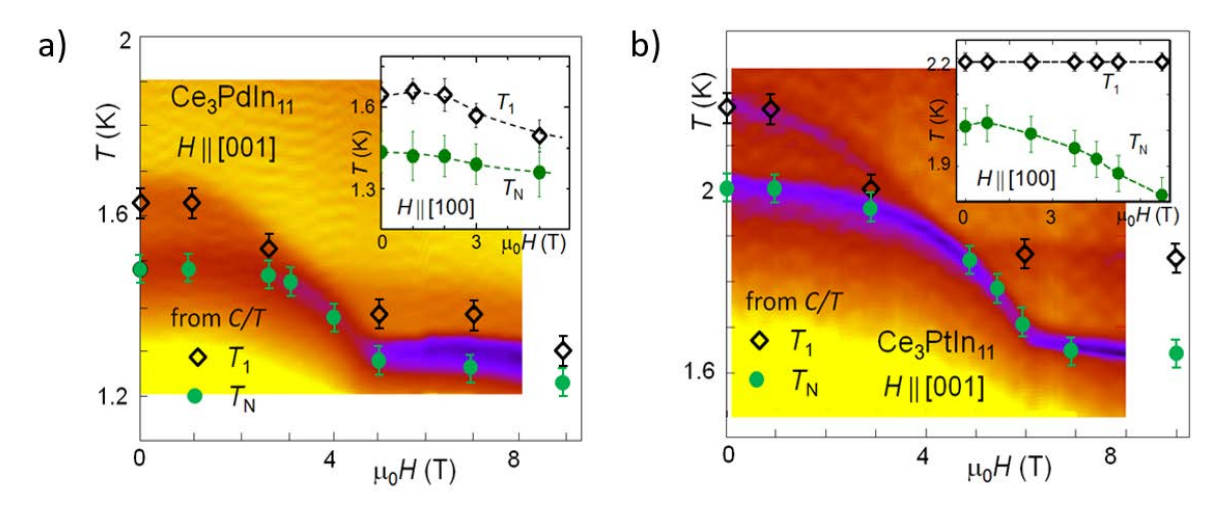


Figure 2: The temperature-magnetic field phase diagram constructed from specific heat measurements of a) Ce<sub>3</sub>PdIn<sub>11</sub> and b) Ce<sub>3</sub>PtIn<sub>11</sub>. The main figure shows the data mapped by the thermal response technique for  $H \parallel c$  and the inset shows data for the  $H \perp c$  axis derived from standard specific heat measurements based on the relaxation technique. The black diamonds and the green circles show  $T_1$  and  $T_N$ , respectively. Data taken from [A4, A5].

Table 1: Comparison of the lattice parameters, transition temperatures  $T_1$ ,  $T_N$  and  $T_c$ , the Sommerfeld coefficient  $\gamma$ , initial slope of  $(d\mu_0H_0/dT)_{T_c}$  and the upper critical field  $H_{c2}$  for Ce<sub>3</sub>PdIn<sub>11</sub> and Ce<sub>5</sub>PdIn<sub>19, D</sub>ata taken from Ref. [A4,A5].

Ce <sub>3</sub> PdIn <sub>11</sub>	Ce <sub>3</sub> PtIn <sub>11</sub>
a = 4.689(6) Å	a = 4.698(8)  Å
c = 16.891(3)  Å	c = 16.874(3) Å
$T_1 = 1.7$	$T_1 = 2.2 \text{ K}$
$T_{\rm N} = 1.5 \; {\rm K}$	$T_{\rm N} = 2.0 \; {\rm K}$
$T_{\rm c} = 0.42 \; {\rm K}$	$T_{\rm c} = 0.32 \; {\rm K}$
$\gamma = 1.7 \text{ J-mol}^{-1} \text{K}^{-2}$	$\gamma = 1.2 \text{ J·mol}^{-1} \text{K}^{-2}$
$(d\mu_0 H_{c2}/dT)_{1T_c} = -12.25 \text{ T/K}$	$(d\mu_0 H_{c2}/dT)_{lT_c} = -8.04 \text{ T/K}$
$\mu_0 H_{c2}(0) = 2.3 \text{ T}$	$\mu_0 H_{c2}(0) = 1.4 \text{ T}$

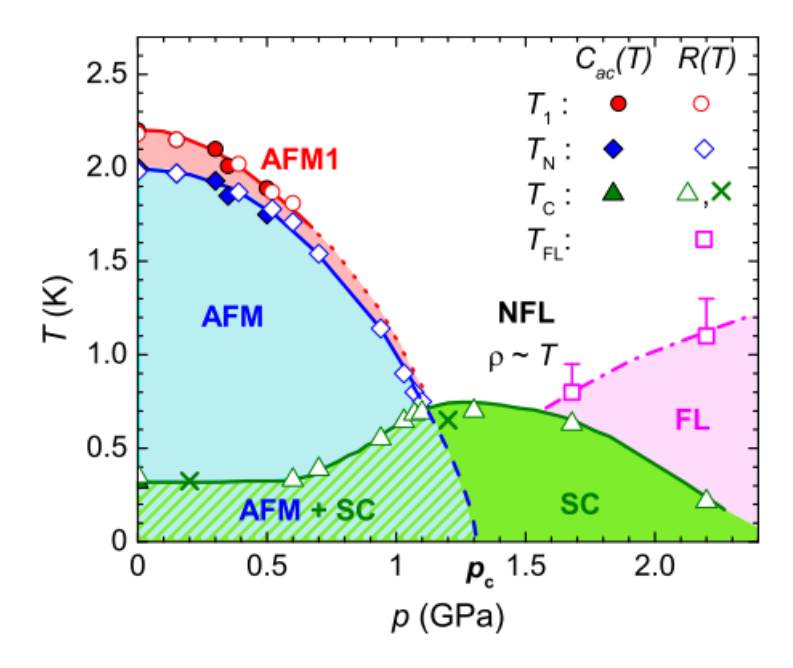


Figure 3: The zero-field T-p phase diagram of Ce<sub>3</sub>Ptin<sub>11</sub>. Transition temperatures  $T_1$  (circles),  $T_N$  (diamonds),  $T_c$  (triangles), and  $T_{FL}$  (squares) obtained from ac calorimetry and resistivity are denoted by closed and open symbols, respectively. The crosses are the results of a sample from different batch. A possible continuation of  $T_1 \rightarrow T_c$  and  $T_N \rightarrow 0$  is indicated by the red-dotted and blue-dashed line, respectively. Taken from [A5].

Our study shows that in Ce<sub>3</sub>PtIn<sub>11</sub> the transition temperatures are slightly higher, see Figure 2 and Table 1. Moreover, the transitions in the specific heat and resistivity data (not shown) are sharper, suggesting better sample quality. Therefore, Ce<sub>3</sub>PtIn<sub>11</sub> was selected for hydrostatic pressure studies. We have performed resistivity and *ac* calorimetry to explore the temperature-

pressure phase diagram; see Figure 3. Similar to other heavy fermion systems, with increasing pressure it shows a gradual decrease of the antiferromagnetic order, while the T<sub>c</sub> is increasing, at pressure of 1.1 GPa the  $T_{\rm N}$  and  $T_{\rm c}$  have the same value. Under pressures between 1.1 and 1.6 GPa, superconductivity evolves out of the non-Fermi liquid state. Maximum  $T_c = 0.7$  K is reached at ≈ 1.3 GPa, indicating the position of the magnetic QCP [14,18]. Similar to Ce<sub>3</sub>PdIn<sub>11</sub> the two crystallographically different Ce(1) and Ce(2) sites are also expected here to experience different Kondo screening. Our [A6] <sup>115</sup>In nuclear quadrupole resonance (NQR) study revealed that the Ce(2) ions maintain their 4 f-magnetic moments due to insufficient Kondo screening. The Ce(2) moments become magnetically coupled via an RKKY interaction through the adjacent Ce(1)<sub>2</sub>PtIn<sub>8</sub> layer, establishing long-range AFM ordering at 2 K. It was shown that the In(4) site surrounding the Ce(2) site experiences internal field also in the superconducting state confirming that the magnetic order persists down to lowest temperatures, therefore, the OCP at pc 1.3 GPa is inherent to the Ce(2) sublattice. In contrast, the Ce(1) ion is on the verge of magnetic ordering, but the enhanced local on-site Kondo interaction just balances out the RKKY interaction. It supports the hypothesis about the spatial separation of magnetism and superconductivity such that the Ce(1)<sub>2</sub>PtIn<sub>8</sub> layer would be primarily responsible for superconductivity and the Ce(2)In<sub>3</sub> layer for magnetism. Another group performed a further symmetry analysis of their <sup>115</sup>In NQR spectra and defined the propagation vectors in the two antiferromagnetic states, and, in a similar conclusion to our previous results, further discussed the role of two inequivalent Ce sites [70].

# 1.3 Summary

Discovery of the Pd- and Pt- based Ce<sub>n</sub>T<sub>m</sub>In<sub>3n+2m</sub> extended the material bases for studies of the interplay between magnetism and heavy-fermion superconductivity. The fact that several studies of Pd and Pt-based compounds were performed on polycrystals shows, that single crystal growth of these compounds is not straightforward as in the case of Co, Rh and Ir base systems. The problems with growth limit the availability of good-quality samples and subsequent studies. We succeeded in the synthesis of the first single crystals of Ce<sub>2</sub>PdIn<sub>8</sub>, Ce<sub>3</sub>PdIn<sub>11</sub>, Ce<sub>2</sub>PtIn<sub>8</sub> and Ce<sub>3</sub>PtIn<sub>11</sub> and presented detailed procedures to obtain phase pure crystals. Subsequently, we performed pioneering experiments on Ce<sub>3</sub>PdIn<sub>11</sub> and Ce<sub>3</sub>PtIn<sub>11</sub> single crystals and disclosed the unique position of the two materials within Ce-based heavy fermion compounds. They exhibit the coexistence of antiferromagnetic order and superconductivity [A4,A5]; moreover, due to the presence of two distinct Ce sites in the crystal lattice, the magnetic order and superconductivity are believed to be spatially separated within the two distinct Ce sublattices.

# 2 Materials for antiferromagnetic spintronics

The majority of spintronic research is naturally conducted on thin films or multilayers from which various sophisticated and complex devices are fabricated. The role of bulk materials is in the determination of their fundamental physical properties and in searching for potentially interesting materials for spintronics applications. In the section below, three different cases of bulk material studies are presented: In the case of CuMnAs, the material was considered as potentially interesting for antiferromagnetic spintronics application; however, there was almost no knowledge about its properties. In such a case, it is often more economical to investigate the basic properties of bulk materials and evaluate whether it satisfies the fundamental expectations. And so it was done as explained below. Similarly, NaMnAs was reinvestigated for possible applications, with the difference that no thin films have been prepared yet for reasons discussed. Another reason why bulk materials are investigated are types of measurements that are difficult or impossible to be conducted in thin films either for the reason, that the experiments require some critical sample volume (such as inelastic neutron scattering), specific crystal orientation, or clean surfaces, as shown for the case of angle-resolved photoemission spectroscopy (ARPES) on altermagnetic MnTe.

# 2.1 Antiferromagnetic Spintronics

With the absence of stray fields in antiferromagnets and inherently faster dynamics (as opposed to ferromagnets), this branch of spintronics holds the promise of commercially viable memory devices [71,72]. The demonstration of a spin-valve-like signal in NiFe/IrMn/MgO/Pt with an antiferromagnetic metal (InMn) on one side and a non-magnetic metal (Pt) on the other side of the tunnel barrier (MgO) showed the possibility of studying antiferromagnetic materials by antiferromagnetic tunnelling anisotropic magnetoresistance [73]. Since then, various concepts have been proposed not only for reading, but also for manipulating the Néel vector in antiferromagnets, which opened the possibility of replacing ferromagnets with antiferromagnets, which being the active spin-dependent element [74,75].

Today, the most popular compounds in AFM spintronics are CuMnAs and Mn<sub>2</sub>Au. Their locally broken inversion symmetry on the Mn sublattices allows manipulation of the magnetic order using the so-called Néel order spin-orbit torque (NSOT) or also called the inverse spin-galvanic effect (ISGE) [76]. In ISGE, the electrical current in a crystal with broken inversion symmetry generates a non-equilibrium spin polarisation. In a (ferro)magnetic crystal, the current-induced spin polarisation exchange couples to the equilibrium magnetic moments and generates a torque. In antiferromagnetic systems, a centrosymetric crystal lattice is required, where opposite polarizations of the magnetic sublattices locally break the inversion symmetry. The torque is generated locally and changes the sign at each sublattice. Predicted by Železný et al., for Mn<sub>2</sub>Au [76], it was shown for the first time in the tetragonal phase of CuMnAs by Wadley et al. [77].

#### 2.2 CuMnAs

Recalling the phrase new physics in old material within the search of room-temperature antiferromagnetic (semi)conductors, the CuMnAs compound was chosen as one of the promising candidates for more detailed study. The compound was reported for the first time by Mundelein and Schuster in 1992 [78] as a stoichiometric MnCuAs polycrystalline material with orthorhombic crystal structure (space group Pnma). Magnetic susceptibility data in a range of 65-282 K suggested antiferromagnetic order above room temperature, which was the first motivation for studying the system further. Combined theoretical and experimental work by Máca et al. [A7] showed that orthorhombic CuMnAs 1 is a room temperature antiferromagnet with a Néel temperature around 330 K. Soon after the confirmation of antiferromagnetic order at room temperature, molecular beam epitaxy was employed to grow thin films. In thin film form, the compound was shown to have a tetragonal Cu<sub>2</sub>Sb-type structure (P4/nmm) with collinear antiferromagnetic order [79]. In CuMnAs, the Mn atoms occupy the 2c crystallographic position and the magnetic symmetry lacks time-reversal symmetry. Together with lattice translation (antitranslation), it makes the material suitable for NSOT; the electrical switching [77,80] and domain wall manipulation made CuMnAs the most prominent compound of antiferromagnetic spintronics.

The connection between the bulk properties and thin-film behaviour had not been presented prior to our work. Most of the spintronic functionality research was clearly performed on thin films, while basic bulk characterisation such as anisotropy measurements of magnetisation, resistivity or magnetotransport measurements including anisotropic magnetoresistance was missing. Moreover, there was a discrepancy between the crystal structures between the thin films and bulk samples. Our bulk orthorhombic samples in the initial study by Máca et al. [A7], were prepared in polycrystalline form by solid-state reaction. As a next step, we focused on bulk single crystal growth for which bismuth flux method was found to be the most suitable [A8, A9]; however, most of our studies were performed using polycrystalline samples and their single crystalline grains (for details see below]). To disclose the relation between the composition and crystal structures, we performed a study of a broader composition range of the Cu-Mn-As phase diagram, focused on the (Cu-Mn)<sub>2</sub>As compositional line. As such, we were able to isolate both the orthorhombic and the tetragonal phases with almost stoichiometric 1:1:1 composition [A10]. We found that the tetragonal structure may exist not only in the thin film form (stabilised by the substrate), but also in the bulk form, stabilised by the stoichiometry [A10]. At the time of that work, several DFT calculations have been done discussing the anisotropy of transport properties of the tetragonal CuMnAs phase. We aimed to study the magnetotransport properties of the tetragonal phase to complement in-plane resistivity studies on thin films reported by Wadley et al., [79]. The Bi-grown samples were not suitable for the

<sup>&</sup>lt;sup>1</sup> In the notation of I-Mn-V compounds, I and V being Roman numerals for the numbers of valence electrons, CuMnAs instead the originally reported MnCuAs by Mundelein and Schuster has been used since.

studies because of the detected ferromagnetic impurities and also Bi veins in the crystals, which would significantly distort the resistivity measurements. Therefore, we [A11] decided to employ the fabrication method using the focused ion beam technique introduced by P. Moll [81] to prepare micro-devices for magnetoresistance measurement. The device for resistivity measurement along the crystallographic axes a and c is presented in Figure 4 a (the entire sample fabrication is shown in the diploma thesis of J. Volný [82]). The crystal composition  $Cu_{1.02}Mn_{0.99}As_{0.99}$  (determined from EDS) was found to be closest to 1:1:1 stoichiometry and still has the desired tetragonal structure. Mounted on a rotating sample holder, the fabricated device allowed us to measure magnetoresistance along both principal directions and the angular dependence of anisotropic magnetoresistance with the magnetic field applied in the ac plane. We succeeded in measuring the temperature dependence of electrical resistance along both principal axes (see Figure 4 b), the measurements confirmed the expected structural anisotropy with  $\rho_{zz}/\rho_{xx} \sim 6$  coming from the layered character of the compounds.

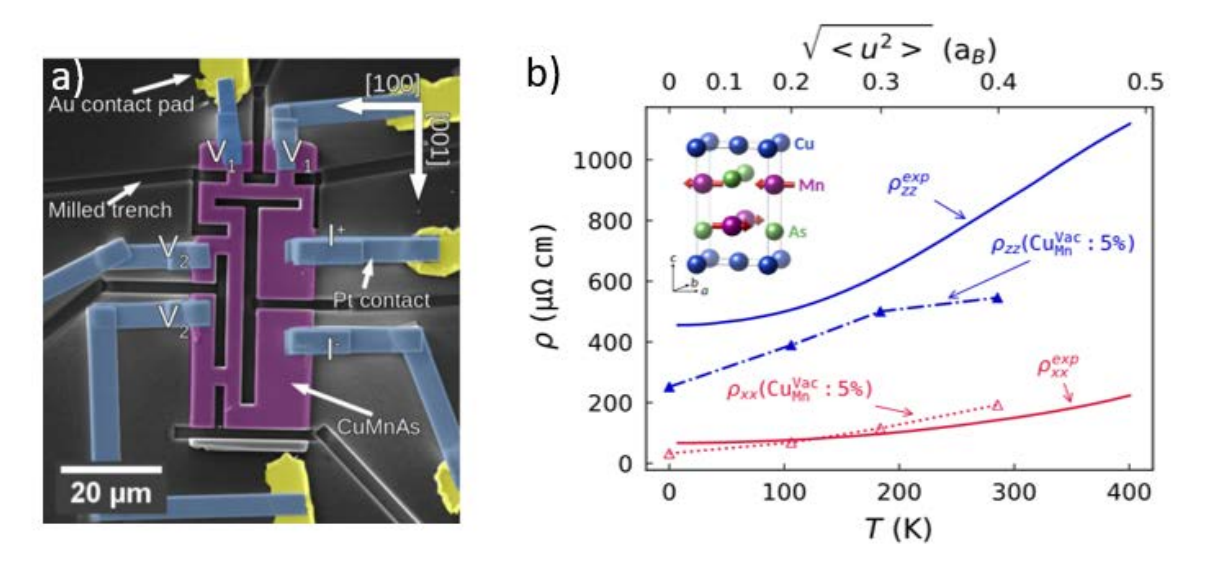


Figure 4: a) False coloured SEM image of the device and the single-crystalline grain from which it was fabricated. The crystallographic directions [001] and [100] correspond to the c and a axes, respectively. The magnetic field H is rotated, with respect to this micrograph, from an in-plane direction H||[100] ( $\psi=0$ ) to an out-of-plane H||[010] ( $\psi=\pi/2$ ); H remains always in the basal plane. b) Resistivity of bulk CuMnAs measured along the a (in-plane,  $\rho_{xx}$ ) and c axes (out-of-plane,  $\rho_{zz}$ ) shown by solid lines; crystallographic axes are defined in the inset. To demonstrate a typical level of agreement with model calculations, resistivity assuming scattering on static impurities (CuVAC as explained later in Sec. IV) and phonons are also shown, taken from Volný et al., [A11].

Compared to finite-temperature *ab initio* calculations, including the impurity model, we find it to fit reasonably well with 5% of Cu substituted for Mn atoms. Finite-temperature ab initio calculations, including the impurity model, show that it well reasonably fits with 5% Cu substituted for Mn atoms. Another important parameter is anisotropic magnetoresistance [80],

which can also be used as readout for antiferromagnetic spintronic devices<sup>2</sup>. The anisotropic magnetoresistance was modest in magnitude ( $\Delta\rho/\rho_0 \lesssim 10^{-3}$  at saturation) with a two-fold symmetry indicating the presence of in-plane uniaxial anisotropy, which could be a consequence of the unequal number of magnetic domains in the microfabricated device.

#### 2.2.1 Exploring the (Cu-Mn)<sub>2</sub>As line of the Cu-Mn-As diagram

The stability of the tetragonal and orthorhombic structures was found to be very sensitive to the composition. We decided to explore the larger part of the compositional line connecting Mn<sub>2</sub>As with Cu<sub>2</sub>As. As shown in Figure 5, there are several crystal structures formed along the line. Within the precision of the SEM EDS analysis (considering the absolute error of 1-2 at. % <sup>3</sup>) we found that Cu-rich crystals are tetragonal, while the stoichiometric and slightly Mn-rich crystals have orthorhombic structure. The border between these two phases was determined as Cu<sub>1.02(2)</sub>Mn<sub>0.99(2)</sub>As<sub>0.99(2)</sub> with the composition closest to the stoichiometric CuMnAs and having the tetragonal structure. For this composition, the highest Néel temperature of 508 K was reached, which is approximately 170 K higher than in the stoichiometric orthorhombic CuMnAs (Figure 5 b).

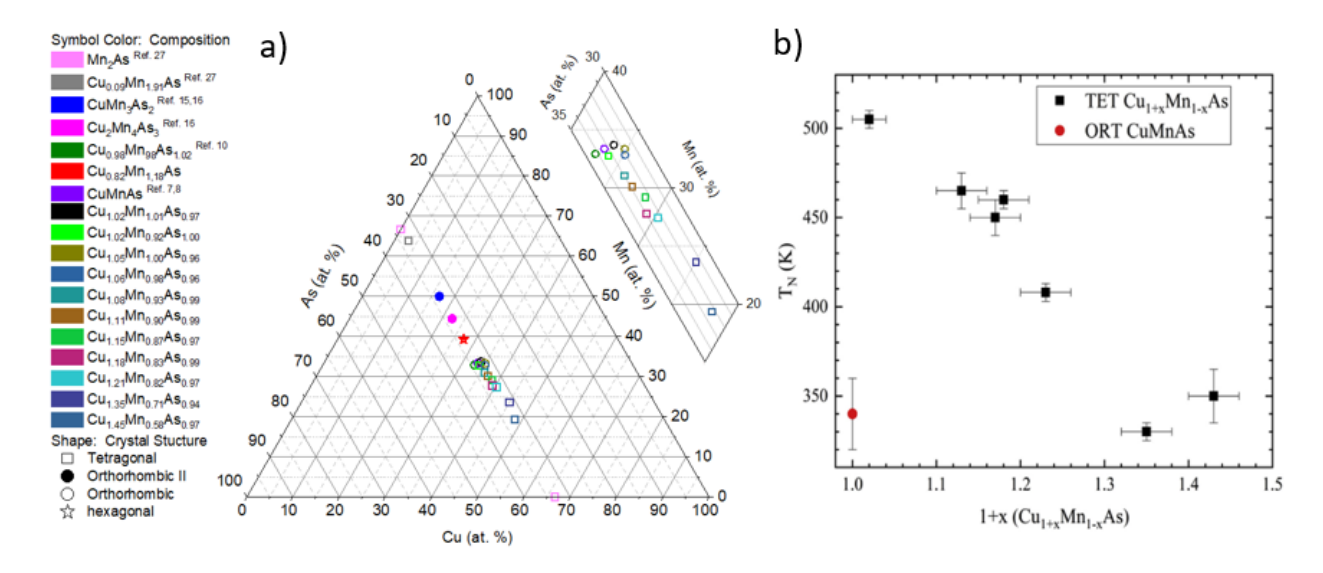


Figure 5: a) Cu-Mn-As ternary diagram. The colour coding refers to different compositions, the tetragonal phase is presented by symbol  $\Box$ , the orthorhombic phase by symbol  $\circ$ , the orthorhombic II phase by symbol  $\bullet$ , and the hexagonal phase by symbol  $\bigstar$ . On the top-right side of the image is a detail on the central part of the diagram. b) The composition dependence of the Néel temperature in tetragonal CuMnAs samples. An updated version from [A10]

Compounds that contain significantly higher amounts of Mn, such as Cu<sub>2</sub>Mn<sub>4</sub>As<sub>3</sub> CuMn<sub>3</sub>As<sub>2</sub>, have orthorhombic structure with double unit cell size (see Figure 6), the phase is labelled as

15

<sup>&</sup>lt;sup>2</sup> For magnetic-based devices, it has been already used in industry for decades

<sup>&</sup>lt;sup>3</sup> Note: Here "at.%" is a unit, therefore speaking about absolute error.

orthorhombic II. There are three crystallographic sites for Mn in this phase, which is reflected in the rather complex magnetic behaviour [A8]. Interestingly, a hexagonal phase with the composition Cu<sub>0.82</sub>Mn<sub>1.18</sub>As was found to exist between the two orthorhombic phases having in-plane triangular magnetic ordering [83].

All of these subtle changes in composition have a strong impact on the crystal structure and magnetic interactions of the Cu-Mn-As alloys. Ab initio calculations for a varied Cu concentration on Mn sublattice showed that the difference between the total energy of the tetragonal and orthorhombic phases is very small and changes sign at concentration Cu<sub>1.05</sub>Mn<sub>0.95</sub>As. Above this value, the energy difference increases monotonically, favouring the tetragonal phase, in agreement with the experimental findings ref. This may have a practical aspect in tuning the magnetic properties by composition. When thin films are made, the composition is more difficult to determine because standard techniques such as electron probe energy dispersive X-ray spectroscopy (EDS) or X-ray fluorescence (XRF) have a penetration depth much higher than the film thickness and cannot provide high accuracy. The XRD cannot sufficiently distinguish between Cu and Mn because of very similar scattering powers. The Néel temperature can then be a good indication for composition variation/tuning in thin films, where the Néel temperature in the range 480 - 485 K [84,85] was close to the maximum value for bulk samples.

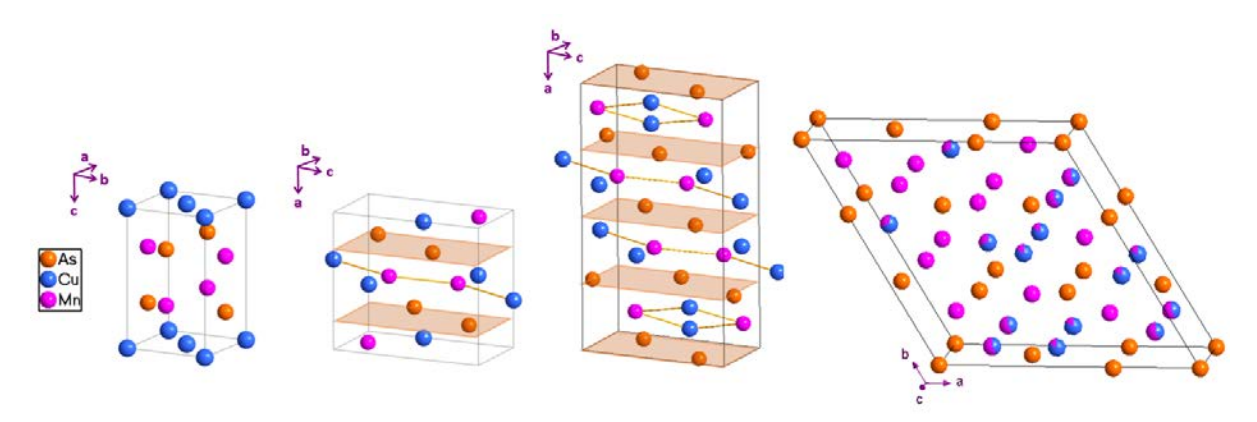


Figure 6: a) Tetragonal, b) orthorhombic and c) orthorhombic II structures of  $Cu_{1+x}Mn_{1-x}As$  compounds. The shaded planes are a guide for the eye, highlighting similarities between orthorhombic cells, taken from [A8].

#### 2.3 NaMnAs

Progress in antiferromagnetic spintronics is likely to be stimulated by the introduction of new antiferromagnetic (semi)conductors with desired physical properties (high Néel temperature, proper band structure, symmetry, etc.). In addition to CuMnAs, a promising group of materials in the group of metal manganese pnictides is the *A*Mn*X* (A=Li, Na, K, X=P, As, Sb, Bi) family [78,86,87]. Most *A*Mn*X* materials order antiferomagnetically with Néel temperatures exceeding room temperatures as shown in the initial study by Bronger et al., [86] In their work, they presented magnetic structures refined from powder neutron diffraction data at several

temperatures. Now, other studies of this system had been done until more than two decades later when they were rediscovered in the scope of antiferromagnetic spintronics [88–91]. Ab initio calculation predicted a band gap in the order of hundreds of meV [88,91]. It was experimentally shown that LiMnAs thin films [88,89] were semiconducting while NaMnBi single crystals [90] were semimetallic with a strong dependence on crystal defects [90].

We focused on single crystal growth and characterisation of NaMnAs and NaMnSb. Both compounds could be prepared using bismuth flux; however, NaMnSb contained too high amount of MnAs impurity phase, which excluded it from further studies.

NaMnAs crystallises in the tetragonal structure (space group P4/nmm) like the AMnX group members (there are, however, different structure types). Compared to CuMnAs, the Mn atoms in NaMnAs occupy the 2a position and form flat planes well separated from each other by the As and Na atoms. Magnetic moments are aligned along the c axis, within the planes they are coupled antiferomagnetically, the interlayer coupling is ferromagnetic [86].

Single-crystal XRD, including reciprocal space mapping (not shown), showed a very uniform composition (sharp peaks) and low mosaicity (1°). The material is easily exfoliable using the Scotch tape method. The easy exfoliation is typical for the so-called van der Waals materials; however, in NaMnAs and related systems, there is no van der Waals gap in the structure, and the bonds are ionic/covalent with high anisotropy of the Young modulus [92]. The preparation of thin layers by exfoliation may bring advantages in the preparation of filed-effect devices; however, we have not tested such a procedure yet. The limitation lies in the reactivity of the sample in air or after annealing. An investigation of the stability of the compound using XRD (see Supplementary material in A12) showed that during the exposure to the air, MnAs grew on the surface while Na reacts with air.

MnAs is a very unsuitable impurity, because it is ferromagnetic and metallic; even a small amount of it has a dominant effect on the magnetic signal (see Figure 7) and conductivity, respectively. We therefore focus on studies where the impurity had less impact, such as XPS and UPS, where only a small in situ cleaved sample area was exposed, or optical transmitivity, where a small amount of impurity does not provide a significant signal. NaMnAs was shown to be a p-type semiconductor with a band gap between 0.9 and 1.16 eV depending on whether it is direct or indirect (both models are shown), respectively. The Néel temperature of 350 K determined from magnetisation measurement is in agreement with previous powder neutron diffraction experiments reporting the presence of magnetic order at 293 K and paramagnetic state at 643 K [86].

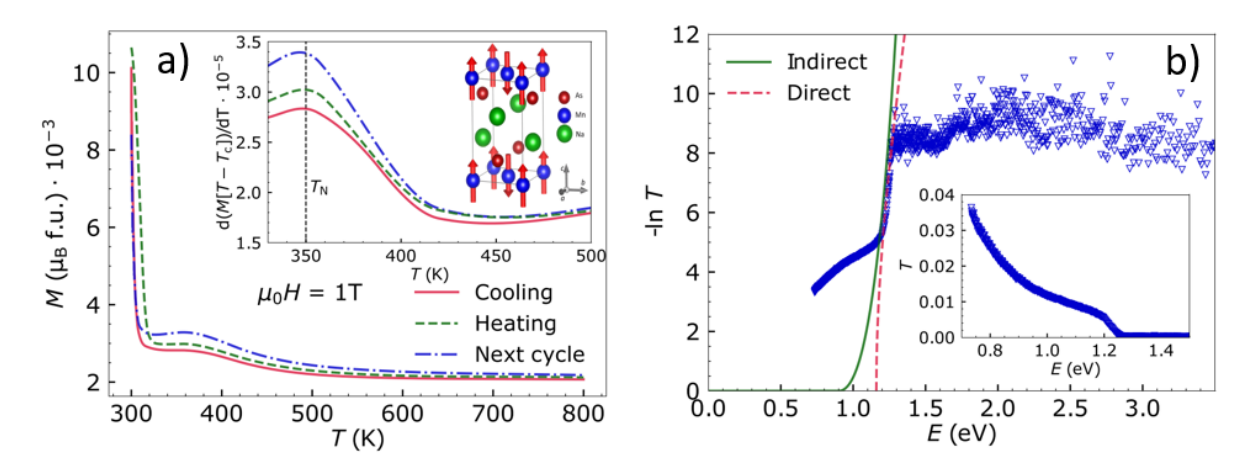


Figure 7: a) Temperature dependence of magnetization. Below 320 K, there is a dominant ferromagnetic signal form MnTe impurity. The inset shows detail on the antiferromagnetic transition of NaMnAs. b) The inset: The spectral dependence of the optical trans mission T. The main plot: The same data replotted as  $ln\ T(E)$  fits in the interval of 1.2–1.4 eV by a direct (red, dashed) or indirect band-gap model allow to estimate the band gap. Taken from [A12].

The investigation of electronic properties were subject to ab initio calculations using local density approximation (LDA) and LDA + U. From LDA, Heisenberg exchange parameters  $J_{ij}$  between two manganese atoms i and j were in agreement with the reported magnetic structure [86], i.e. they resulted in antiferromagnetic exchange coupling between the nearest neighbours, ferromagnetic coupling between second nearest neighbours and ferromagnetic interlayer coupling. The calculated intra-layer exchange interactions are much stronger than the inter-layer ones reflecting the 2D-like arrangement of the Mn atoms. To investigate this highly anisotropic exchange parameter experimentally, we have been focused on probing magnon spectra infrared magneto-transmission spectroscopy in a wide temperature range and up to magnetic field of 30 T. The data show a strongly two-dimensional character of the magnons, with magnon energy significantly higher than it was calculated. This provides interesting playground for THz-based applications/research operating at room temperature (in preparation [93]).

Magneto transport properties, which would probe the material's anisotropy, have not been studied due to the presence of conducting impurities, mainly MnAs, which appeared difficult to remove. Current trends with air sensitive van der Waals materials that can be exfoliated and encapsulated under hBN or mica [94,95], can be a solution for further studies of NaMnAs under controlled conditions. Such procedure would allow to fabricated more sophisticated devices including above mentioned THz based applications or applying of variable gate voltages in order to control the magnetic anisotropy by electric field [96].

.

## 2.4 MnTe – the first experimentally confirmed altermagnet

An emerging field in antiferromagnetic spintronics is compensated collinear antiferromagnets with broken *PT* (parity and time-reversal) symmetry, the so-called altermagnets. In altermagnets, the spin angular momenta are fully compensated but due to the crystal lattice, the spin lattice has the broken PT symmetry [97,98]. MnTe (α-MnTe<sup>4</sup>) is an exemplary model for studying altermagnetism at room temperature. It is well-established antiferromagnetic semiconductor (commonly p-type) with a hexagonal structure (space group P6<sub>3</sub>/mmc) that has been investigated since the 1960s [99] for different application such as antiferromagnetic spintronics [75,100–102]. Recently, it has been in the spotlight due to its magnetic symmetry [103]. It consists of two sublattice of Mn atoms, whose magnetic moments align antiparallel below the transition temperature of 310 K. These sublattices are linked by a non-symmorphic six-fold screw-axis rotation, rather than through translation or inversion symmetries, which is the main prerequisite for altermagnetism.

The unique electronic properties of MnTe, arising from its altermagnetic nature, exhibit both weak and strong altermagnetic spin splitting. The weak spin splitting occurs along four high-symmetry (nodal) crystal planes and is facilitated by weak spin-orbit coupling (SOC) in this centrosymmetric material [2]. In contrast, strong spin splitting is observed outside these nodal planes and does not rely on SOC. To investigate these specific altermagnetic electronic properties in MnTe within three-dimensional reciprocal space, Spin- and Angle-resolved Photoemission Spectroscopies (SARPES) are the preferred method. In Krempaský et al., [A13], we directly demonstrated both the weak and strong lifting of Kramers' spin degeneracy in the band structure of MnTe.

We utilized a combination of MBE-grown MnTe thin films and MnTe crystals to characterize the strong altermagnetic splitting observed outside the nodal plane at  $k_z \approx 0.12~\text{Å}^{-1}$ . This was measured using soft-X ARPES at photon energies of 368 eV for the epitaxial films and 24 eV for the cleaved crystals, respectively. This choice of samples was necessary because SARPES measurements could only be conducted in the UV-ARPES regime using cleaved crystals. Preparing samples from 3D crystals like MnTe can be quite delicate. However, our cleaved MnTe provided high quality surface from which SARPES data in [A13] demonstrated strong altermagnetic splitting around 0.7 eV, aligning well with theoretical predictions.

Additionally, the unusual shape of the 2D Fermi surface observed from the cleaved surface also matched theoretical expectations. Unlike the six-fold symmetry Fermi surfaces measured from thin epitaxial films, our data from cleaved crystals indicated a single-domain state with the Néel vector aligned along the easy axis corresponding to the MFM direction. These experimental results were corroborated by theoretical calculations assuming a single-domain state with the Néel vector aligned along the easy MFM axis, as previously suggested by X-ray diffraction studies of the pristine  $\alpha$ -MnTe (0001) surface. Interestingly, the six-fold symmetry

\_

<sup>&</sup>lt;sup>4</sup> Further only MnTe because the other phases are only stable at temperature above 900°C.

Fermi surfaces observed from the thin epitaxial films and associated ARPES cuts along the K $\Gamma$ K direction displayed characteristic quadratic band dispersion, resulting from the presence of three Néel domains. This was in excellent agreement with the weak altermagnetic spin splitting driven by SOC in the  $k_z$  = 0 nodal plane of MnTe.

In conclusion, ARPES study of MnTe crystal confirmed characteristic 2D Fermi surface structure from a single-domain state. Similar maps were very recently measured from single-domain patterned MnTe thin film surfaces [104], which opens a new perspective for altermagnetic applications for spintronics [105,106]

# 2.5 Summary

We have presented several bulk studies of antiferromagnets with potential spintronics applications and showed that bulk studies can effectively support the characterisation of materials usually prepared in thin films. In the case of CuMnAs, the initial confirmation of the room-temperature antiferromagnetic order led to the thin-film growth of one of the most studied antiferromagnetic spintronic materials. Another important contribution was the study of the composition-phase diagram, which showed the relation between the stoichiometry and crystal structure. Not only in this case, the bulk studies allowed to determine more precisely (and cheaper) than in the thin-film materials. The growth of NaMnAs single crystals allowed us to study its band gap for the first time, to confirm its semiconducting behaviour and the unusually strong single-ion anisotropy of Mn atoms. Its layered structure motivates us to consider the fabrication of devices from exfoliated flakes. Last but not least, MnTe single crystals allowed, for the first time, to prove the altermagnetic splitting of Kramer's doublet. The soft-X APRES and SARPES measurements at photon energies of 24 eV with extremely low penetration depth ( $\approx 5$  Å) were only possible to measure on an *in situ* cleaved crystal with perfectly clean surface.

# 3 Misfit layered compounds as candidates for sliding ferroelectricity

The misfit layer compounds belong to two-dimensional (2D) van der Waals materials. Since the discovery of the atomically thought layer of graphite, graphene, 2D materials have attracted much attention for their fascinating properties and are promising candidates for the fabrication of complex electronic devices [107–110]. The variety of materials studied increased substantially and provided a variety of magnetic [111] and ferroelectric materials [112,113], semiconductors, insulators [114] or superconductors [115]. The most advantageous feature is the weak van der Waals (vdW) interactions, which allow a physical assembly of several functional layers that do not rely on one-to-one chemical bonds and, therefore, are not limited to materials that have similar lattice structures or require compatible synthetic conditions [95,108,116–118]. Methods have been developed to create artificial materials that combine layers with different properties have been developed; however, the preparation of artificial heterostructures is tedious work. The individual monolayers are exfoliated and then placed on top of each other in a correct arrangement. This brings about inevitable problems with the reach of clean atomically flat interfaces and with reproducibility.

# 3.1 Ferroelectricity in van der Waals materials

The ferroelectricity in van der Waals materials is principally different from conventional metal oxide ferroelectricity known for more than 100 years [119]. In conventional ferroelectrics, polarisation is induced by ionic displacement, on the other hand, in 2D van der Waals materials, polarisation is induced by specific stacking of layers [120]. Within van der Waals materials, several intrinsically polar structures have been discovered, such as  $CuInP_2S_6$  (CIPS) [121] or  $\alpha$ -In2Se3 [122,123].

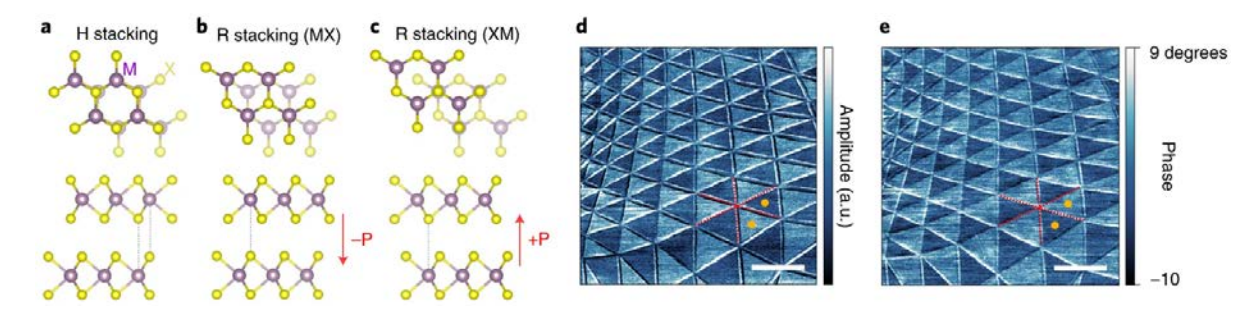


Figure 8: a) Hexagonal (nonpolar) stacking of a TMD. b) MX and c) XM rhombohedral stacking of TMD bilayers with depicted polarisation direction. Images taken from the work of Wang et al., [124].

In 2017, Li and Wu proposed [114,125] that out-of-plane polarisation should be universal for all 2D materials if properly stacked. The van der Waals materials with non-polar structure can be turned into polar (ferroelectric) materials when the layers are slid or twisted, which brakes

the inversion or mirror symmetry. This was experimentally demonstrated in hexagonal boron nitride (hBN) [112,116,126] on MoS2 [117] or transition metal dichalcogenide (TMD) heterobilayers [113] that in the reconstructed moiré lattice, a triangular form with out-of-plane polarisation is formed. The difference between the stacking of the hexagonal and polar rhomboedral bilayers is presented in Figure 8 a-c. Figure 8 d and e represent typical AFM tapping mode amplitude and phase image, respectively, of sliding ferroelectric domains that have almost regular triangular forms. The triangular shape of the domains is a consequence of reconstruction of the hexagonal moiré lattice [127], the periodicity of the moiré superlattice am  $\approx$  a/ $\theta$  (a being the lattice parameter of the material and  $\theta$  the small twist angle); however, quite often they are distorted due to strain [112,116,117,126,127].

Many other twisted heterostructures of graphene, hBN or TMDs have been investigated [128,129]. As recently shown by two independent teams in the Science journal, twisted MoS<sub>2</sub> [130] and parallel-stacked hBN [131] show ultra-fast fatigue-free switching. The switching mechanism in sliding ferroelectrics is different from the polarisation switching mechanism in conventional ferroelectrics, the polarization is switched by mutual interlayer sliding or twisting. No defects are generated over time with switching cycles. Sliding ferroelectrics are therefore of great interest for applications as non-volatile memory devices [130,131].

## 3.2 Discovery of sliding ferroelectricity in MLCs

### 3.2.1 Misfit-layered compounds

The fabrication of artificial superlattices is a tedious task, and the reproducibility of fabricated devices is often insufficient [129]. This is not only due to the precision of the transfer, but also to the limitations to obtain reasonably clean interfaces [129,132]. Layered materials consisting of naturally grown superlattices, misfit layered compounds (MLCs) [133], have on the other hand, atomically clean interfaces.

MLCs are thermodynamically stable natural van der Waals superlattices formed by layers of MX and  $TX_2$  that are alternately stacked along the c axis, as shown schematically in Figure 9 Schematic picture MLC. The rock salt type MX layer is stacked with transition metal dichalcogenide layer TX2 results in an incommensurate latticeFigure 9. Charge transfer between layers is believed to stabilise the compounds [133–135]. A schematic view of the formation of the lattice is presented in Figure 9. Within the basal plane the MX and  $TX_2$  are incommensurate due to different lattice parameters of each layer; however, their crystallographic axes are usually parallel. The incommensurability of their lattice parameters is reflected in the value of  $\delta$  in the composition. Their general formula can be written as  $[(TX)_{1+\delta}]_n(MX_2)_m$  where T = Ti, V, Cr, Nb or Ta and M = Sn, Pb, Sb, Bi or RE and X = S or Se, which gives a wide spectrum of different materials with different properties, including insulators, semiconductors, superconductors, or magnetic materials [133,135–141].

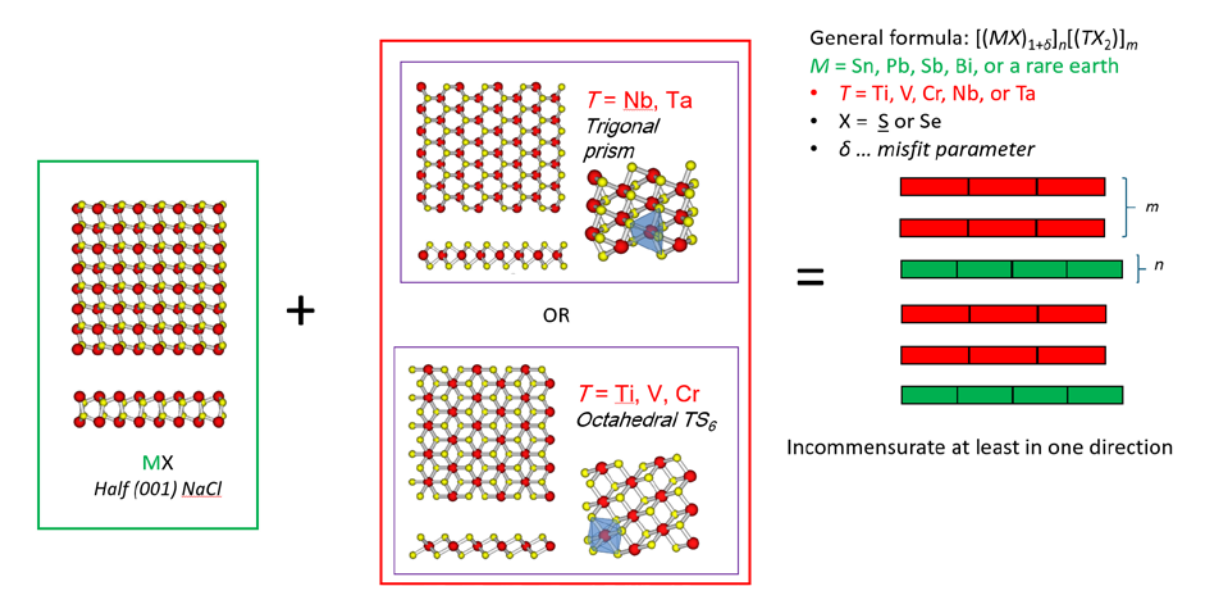


Figure 9: Schematic picture MLC. The rock salt type MX layer is stacked with transition metal dichalcogenide layer  $TX_2$  results in an incommensurate lattice along (at least) one direction due to different lattice parameters of each layer.

#### 3.2.2 Sliding Ferroelectricity in (PbS)<sub>1.11</sub>VS<sub>2</sub>

Our motivation to study MLCs was their unique structure and potential coming from the ability to combine materials properties. We focussed on combinations of layers that could be potentially magnetic, such as VS<sub>2</sub> and CrS<sub>2</sub> and semiconducting such as PbS, in order to find a suitable material for fabrication of charily polarised light-emitting devices (LEDs) similar to MoS<sub>2</sub>/WSe<sub>2</sub> heterostructures [142]. The first crystals, which we prepared, were (PbS)<sub>1.11</sub>VS<sub>2</sub>. Only a few studies on (PbS)1.11VS2 have reported basic evaluation of crystals structure, semiconducting properties [143,144] or STM studies of structural modulation suggesting the presence of charge density waves [145]. Therefore, we focused on revising the crystal structure by detailed single crystals XRD. An important characteristic for potential device fabrication was the surface stability of the compound. We performed SEM and atomic force microscopy measurements on freshly and aged crystal surfaces. We observed features on the surfaces with subnanometer height differences, similar to what is presented in Figure 10. The surfaces remained mostly unchanged even after a few weeks (see the Bc thesis of K. Tetalová [146]). The interesting atypical shapes of the surface domains could not be simply ascribed to step edges of cleaved surfaces; however, as we found soon after, they resembled the moiré ferroelectric domain structures of twisted hBN and TMDs reported for the first time in the same year [112,116,117,126]. Therefore, our work focused on an important breakthrough, to demonstrate that the (PbS)<sub>1.11</sub>VS<sub>2</sub> was sliding ferroelectric as presented in the diploma thesis of K. Tetalová [147] and our manuscripts [A14,A15], similar to the twisted bilayers of TMDs.

In Figure 10 we can see a comparison of different cleaved surfaces of (PbS)<sub>1.11</sub>VS<sub>2</sub> with domains having different sizes and shapes. In Figure 10 a, an area of  $250 \times 250 \,\mu\text{m}^2$  imaged by SEM shows a variety of domain sizes and shapes that can be found in the randomly cleaved sample. In Figure 10 b, a large triangular domains with lateral dimensions of tens on micrometres can be found. This scale correspond to twist angle of  $0.01^{\circ}$ . On the other hand, the 100 nm can be also seen on some of our samples (not shown) that corresponds to  $\theta \approx 1^{\circ}$ . We need to remember that we work with natural samples with large variety of twins and that during cleavage, the sample is deformed inducing additional strain, both factors that influence the domains' sizes and shapes, and we see domains with irregular shapes.

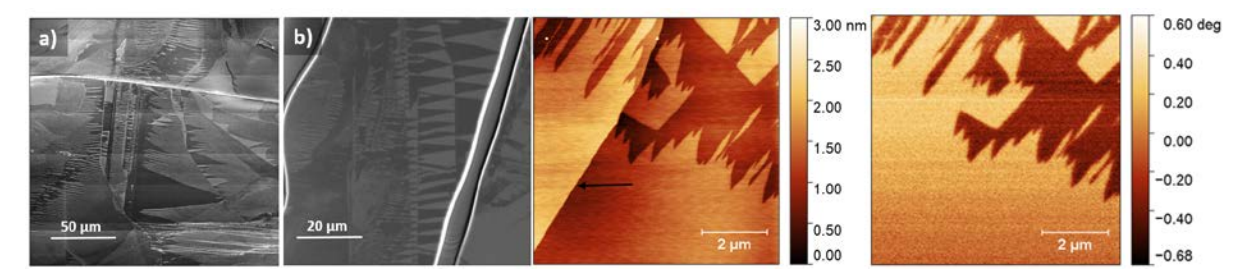


Figure 10: a) SEM image of cleaved sample showing a typical large variation of the domains, and b) another part of the sample showing the triangular domains typical for moiré reconstruction with AB and BA stacking. c) AFM topography image of an area with two types of steps – a step edge marked by the arrow and the height contrast of the domains, and d) a lift-mode phase contrast (EFM) of the same area: while the domains are clearly visible, the step edge disappeared.

To uncover the mechanism of moiré domain formation, we performed detailed single-crystal diffraction measurement and evaluation. It showed that twins are grown with preferably 2H or 3R stacking and that those twins have a small twist angle with respect to each other. Such twins have the potential to form a moiré pattern, which is not present in common transition-metal dichalcogenide crystals. Furthermore, transmission electron microscopy (TEM) provided a local view to the twin formation.

Unlike TMDs made up of identical layers, (PbS)<sub>1.11</sub>VS<sub>2</sub> is a composite system made up of stacking two different layers, which means that after cleaving, different surface terminations (PbS or VS<sub>2</sub>) could be expected. This could explain the height contrast combined with the electric force microscopy (EFM) image in Figure 10 c and d, respectively. Energy-filtered PEEM image of domains of in situ cleaved (PbS)<sub>1.11</sub>VS<sub>2</sub> crystal combined with element map, however, excluded different sample terminations to be responsible for the domain formation [A14]. This leads us to conclusion that sliding ferroelectricity can be observed in cleaved (PbS)<sub>1.11</sub>VS<sub>2</sub> crystals. The mutual interaction between the PbS and VS<sub>2</sub> subsystems allows formation of numerous twins responsible for formation of reconstructed morié lattice that can created polar interfaces depending on the type of stacking [A14].

#### Piezoresponse force microscopy

The key function of ferroelectric materials is their ability to switch the polarisation, i.e., by applying external fields, the polarization direction of a ferroelectric material can be reversed. While in conventional ferroelectric materials, the nonzero polarization is induced by ionic displacement, the polarization in 2D materials is created due to the stacking of the layers. The ferroelectric polarisation can thus be switched by mutual interlayer sliding or twisting. The ferroelectric switching fields in sliding ferroelectric materials are ultralow due to the low interlayer sliding energy barriers [148,149]. The different stacking arrangements of the layers can also be presented as stacking faults. Unlike atomic displacements in conventional ferroelectrics, stacking faults are represented by edge dislocations. These dislocations must be considered when the polarization is switched. It was demonstrated already in the 1960s on graphite [150] and recently on twisted bilayer MoS<sub>2</sub> [117], that the stacking order domain network is topologically protected, as the Burgers vector in 2D layers cannot annihilate freely. Annihilation of the Burgers vector is only possible at the edge of the sample, at a grain boundary [151], or when uniaxial deformation is present [152].

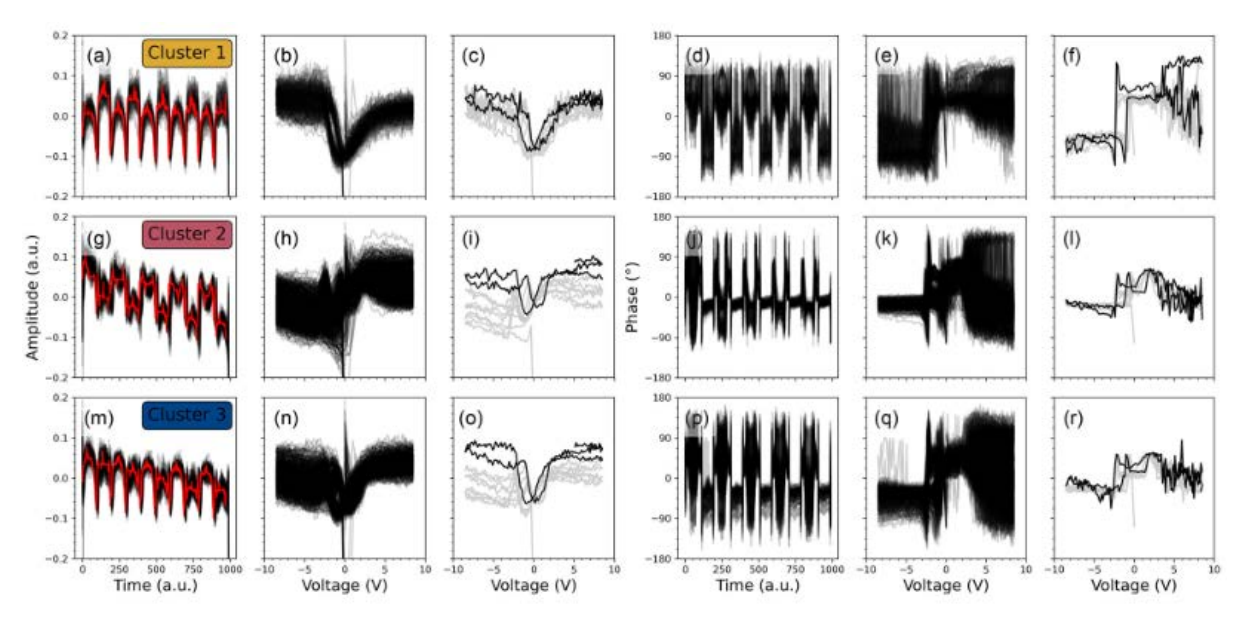


Figure 11: All hysteresis loops measured in a freshly cleaved sample area of  $10 \times 10 \, \mu m^2$  sorted using the k-means clustering method. The first column (a, g, m) shows the amplitude time series of the three clusters. In black, all the hysteresis loops matching the specific cluster are plotted, and in red, the specific centroid. In the second column (b, h, n), the amplitude time series of the first column is plotted as a traditional amplitude–voltage hysteresis loop for all hysteresis loops in the map classified as a similar cluster. The third column (c, i, o) shows one hysteresis loop for each cluster, with the first sweep plotted black and the subsequent sweeps grey. Columns four to six show the respective behaviour of the phase of each cluster: in the fourth column (d, j, p) the phase time series, in the fifth column (e, k, q) the phase versus voltage for all loops classified as the same cluster, and in the sixth column (f, l, r) the phase versus voltage for one hysteresis loop. Taken from Ref. A15.

It is worth to mention that unlike conventional ferroelectrics, the 2D ferroelectrics are not only insulators, but they can also be semiconducting or even metallic. This is also the case of  $(PbS)_{1.11}VS_2$ , which has relatively low resistivity  $(0.1m\Omega cm^{-1})$ . As such, most methods used for studies of conventional ferroelectrics cannot be used. Despite that, we tested piezoresponse force microscopy (PFM) and spectroscopy to characterise the domains [A15]

Analysing several hundreds of measured hysteresis loops different switching behaviour of the domains was identified using machine learning tools (see Figure 11). After the hysteresis loop mapping, the surface appeared to contain a high density of dislocation lines. The different switching behaviour from full switching to nonswitchable areas is therefore believed to be connected with the type of dislocation structure in the PbS layer (Correa2) The behaviour of the majority of loops indicates that the dislocation lines in the PbS layer play a significant role in the possible breaking of the topological protection. The presence of screw dislocations in Figure 2, together with measured hysteresis loops, suggests that dislocations in the (PbS)<sub>1.11</sub>VS<sub>2</sub> compound could break the topological protection and enable switching of the polarization.

#### Domain writing in (PbS)<sub>1.11</sub>VS<sub>2</sub>, using electron beam lithography

Although exposure to electron beams has been proven to switch polarisation of conventional ferroelectric materials [153–155], in sliding ferroelectrics, the conductivity prevents the surfaces from accumulating charges after exposure by electron beams. However, recent work on Y-doped InSe showed that the electron beam induces layer sliding as a result of charge trapping. This should be possible due to the low energy barrier between layers of the siding energy barrier [156].

d) Typical 'force-distance' curve in contact mode AFM, with denoted used set-points e) Contact mode AFM topography and f) trace g) retrace signal in friction mode. The inset shows see-through intrinsic domains in an electron-beam patterned area.

In our work [A16], we tested different parameters for the domain writing and performed a detailed characterisation of the written patterns using TM-AFM and CM-AFM measurements; results of dost-test is presented in Figure 12 for illustration. Subsequently, we discuss whether the observed postexposure patterns can be result of electron-beam-induced polarisation reversal.

Typical factors such as hydrocarbon contamination or local heating, which could misinterpret the data, were excluded based on the character of the written domains. We use two main arguments to support polarization switching in the exposed areas. The first one is connected observation of relatively mobile dislocation lines that run between the exposed patterns as presented in Figure 13.

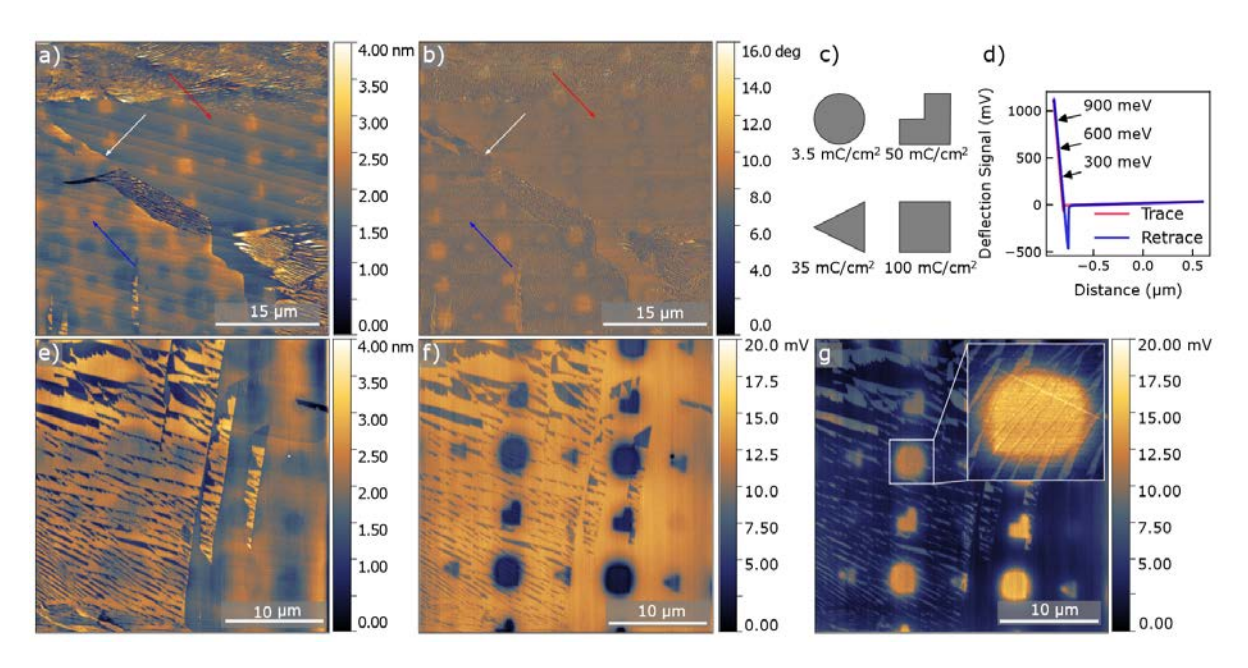


Figure 12: a) Tapping-mode AFM (TM-AFM) topography of exposed sample's surface, b) TM-AFM phase image of the same area, c) the exposure parameters coded in the pattern, 20 keV beam was used

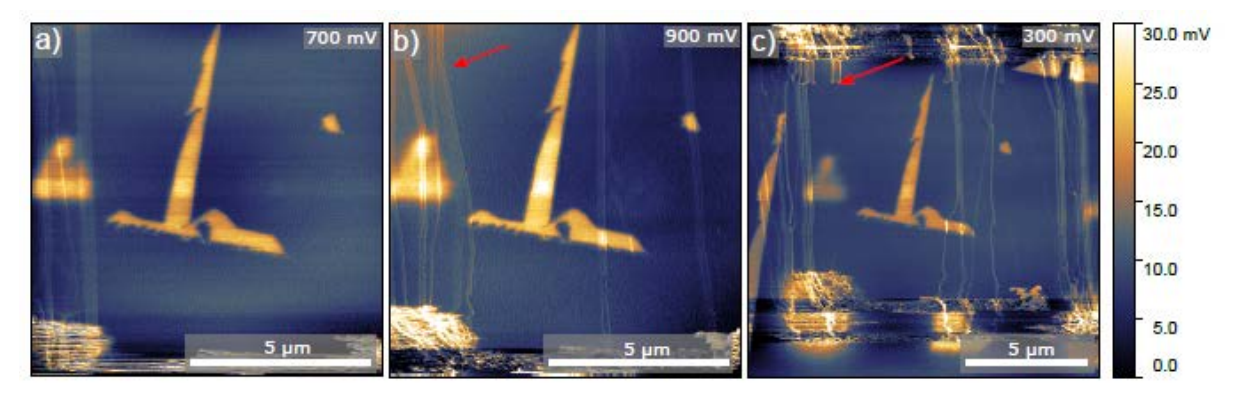


Figure 13: Retrace images of the friction mode of the same area with set points of 700 mV (a), 900 mV (b), and 300 mV (c). The red arrow shows the vertical moving lines propagating from the highest exposed area.

Second, at the polarised areas, a higher nanoparticle density was selectively formed. The nanoparticle growth is connected to our study (see below) showing that the ferroelectric surface can catalyse the growth of hydrocarbon-based nanoparticles, which are selectively formed on specific intrinsic moiré domains [A17]. It can be speculated whether the higher particle density growth can be ascribed to the larger polarisation of the electron-beam pattern or whether the electron-beam pattern inducing an unknown surface modification catalyses the particle growth. However, the electron-beam pattern is not homogeneous in the sample. Such nonpolarisable areas were also shown in our PFM study [A15]. All of this supports the written claim that the electron-beam pattern is ferroelectric domains.

#### **Catalytic functionality**

We would like to present another functionality of (PbS)<sub>1.11</sub>VS<sub>2</sub>, the catalytic function. In ferroelectric materials, spontaneous polarisation can be controlled using various external stimuli, such as a variation in the temperature, light illumination, or an external electrical field. A variation in the sample temperature will change the permanent spontaneous polarisation, the pyroelectrically effect, and thereby also the surface charge density. The positive and negative charges at the surface can part

icipate in a redox reaction at the surface. This pyrocatalytic reaction has been shown to happen when thermal cycling ferroelectric nanoparticles thermally cycling, for example, degrade the rhodamine B dye [157,158], generate H<sub>2</sub>,23 reduce CO<sub>2</sub> [159] or create reactive oxygen species [160]. Similar catalytic reactions in ferroelectric materials can be triggered by mechanical vibrations, the piezoelectric effect [161], or light can also control catalytic reactions in ferroelectric materials [161,162].

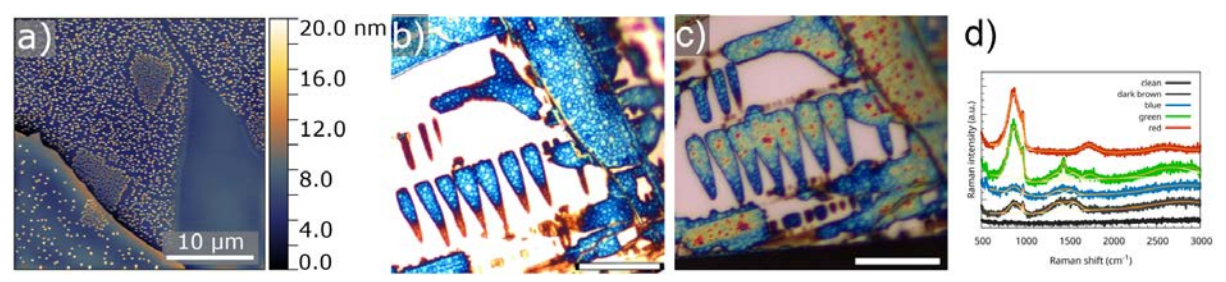


Figure 14: Formation of particles. a) AFM topography image of the cleaved surface with naturel ferroelectric domains and a pattern exposed by the electron beam. b) and c) optical image of a sample surface taken a few months after cleavage. The difference between b and c is two months, and all samples were kept under ambient laboratory conditions d) Raman spectra from areas of samples with different colours (levels of reaction).

At the beginning, we mentioned that the cleaved surfaces remained unchanged for several weeks, as also shown in the Bc thesis of K. Tetalová [146]. Later, we realised that some parts of the samples become contaminated by particles, while other parts remained clean, as shown in Figure 14. In the AFM topography (Figure 14 a), contamination can already be visible after a few days after sample preparation, and later contrast in the optical microscope can also be seen as presented in Figure 14 b and c. On a time scale of weeks to months after cleaving the crystals, the areas gradually change colour (Figure 14 b and c). First, the areas became light brown, then gradually turned to dark brown and subsequently dark blue, light blue, yellow, and red. These regular-shaped areas resemble the shapes of ferroelectric domains (see Figure 10) which led us to hypothesise that the catalytic reaction takes place on one of the domain polarisations. Although the full reactions that take place at the sample are not known, several possible reactions can be identified if we assume that both alkane chains, which are typically present on the surfaces of 2D crystals [163,164], and water are present at the sliding ferroelectric domains. Ferroelectrics are known to show that on negatively charged domains,

'contaminants' (H2O and hydrocarbons) can be reduced to anions (O, OH, COOH, etc.), while adsorption of the 'contaminants' with a polar head (R-OH, R-COOH, etc.) can occur on positively charged domains [165], AFM microscopy does not show signs of degradation of the clean surface between particles, therefore the anions most likely react with adsorbed molecules on the positively charged domains. Raman spectra measured from different areas support the hypothesis that alkane chains, dehydrogenate. Additionally, we have shown that the speed of the catalytic reaction can be substantially increased by white-light illumination. The role of electron beam exposure discussed above is to change the surface functionality, not to stimulate the reactions itself because we see that the sample remains particle-free for several tens of hours after exposure.

### 3.3 Summary

We have performed pioneering experiments showing sliding ferroelectricity in bulk misfit layer compounds and opened discussion about further functionalities. We believe that it will have a broad impact on the physics community and might open a new direction in moiré materials. We try to introduce the concept of van der Waals superlattices as a new moiré generator and to show the potential of the large class of misfit layer compounds as a fascinating playground for exploring moiré physics. The possibility of steering interaction-driven twist angles in bottom-up growth can provide a new pathway to create large-scale moiré landscapes and twintronics, both in thin films and bulk crystals, and might remove the need for manually stacked devices.

# 4 Samples, the essence of materials research

In our laboratory, several methods are available for preparation of polycrystalline and single-crystalline samples: Arc-melting, modified triarc Czorchralski method, Bridgman method using induction or resistive furnaces, laser-heated and halogen lamp heated floating zone method,, flux growth method and chemical vapour transport method. The choice of the method for preparation of specific parameters depends on thermodynamic factors such as phase stability, melting points or vapour pressure of the constituent elements, the reactivity of used elements with growth-a container, and also the desired form of the crystals, and balance with the growth economy. In this chapter, we shall therefor mention the growth condition for selected compounds. Without giving a review of each method, which can be found elsewhere, we present a description of the growth of the above discussed materials. In addition to the growth method, we also like to give introduction to a technique which we implemented in our group, the microfabrication using FIB milling.

### 4.1 The route to quality single crystals

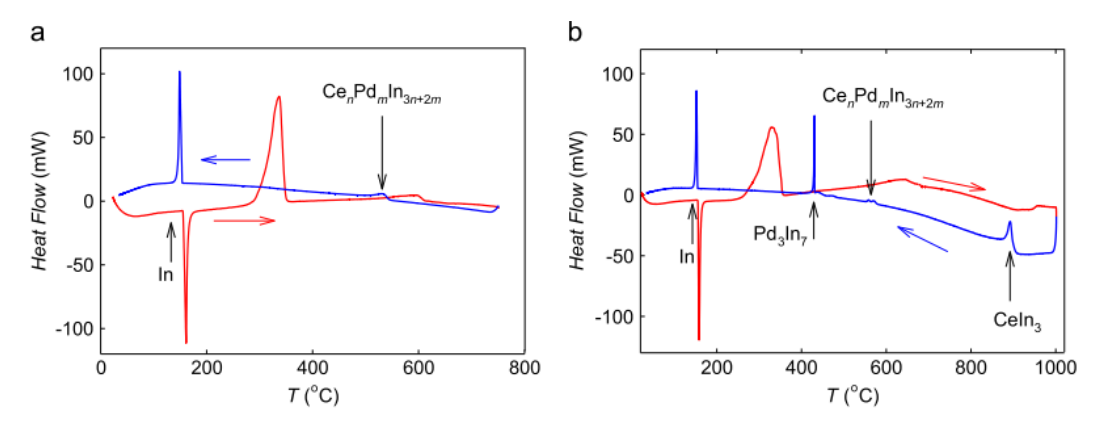
Although having high-quality samples is one of the most important conditions for successful material research, crystal growth and sample preparation are usually limited to a few sentences in the experimental section of the published articles. Therefore, we focus on crystal growth of materials that cost more effort than simply reproducing previously reported recipes. Several materials, such as the heavy fermion superconductors Ce<sub>2</sub>PdIn<sub>8</sub>, Ce<sub>3</sub>PdIn<sub>11</sub>, Ce<sub>2</sub>PtIn<sub>8</sub>, Ce<sub>3</sub>PtIn<sub>11</sub> and antiferromagnetic CuMnAs, or NaMnAs, were prepared in their single crystalline form for the first time; other material such as MnTe had been prepared many times before. However, additional effort was needed to obtain a suitable sample for all of the planned experiments.

In our laboratory, several methods are available for the preparation of single-crystalline and polycrystalline samples. Arc-melting, modified triarc Czorchralski method, Bridgman method using induction or resistive furnaces, laser-heated and halogen-lamp-heated floating zone method,, flux growth method and chemical vapour transport method. The choice of the method for preparation of specific parameters depends on thermodynamic factors such as phase stability, melting points, or vapour pressure of the constituent elements, the reactivity of the used elements with the growth container, and also the desired form of the crystals and balance with the growth economy. Without giving a review of each method, which can be found elsewhere, we present a description of the growth of the materials discussed above.

#### Growth of Ce<sub>n</sub>Pd<sub>m</sub>In<sub>3n+2m</sub> and Ce<sub>n</sub>Pt<sub>m</sub>In<sub>3n+2m</sub> compounds

The series of  $Ce_nPd_mIn_{3n+2m}$  and  $Ce_nPt_mIn_{3n+2m}$  consist of several compounds with different layer stacking. The self-flux method has been used inspired by previously grown CeTIn<sub>5</sub> and Ce<sub>2</sub>Tin<sub>8</sub> compounds (T = Co, Rh, Ir). However, in comparison to these, the Pd- and Pt-compounds are difficult to prepare. Although a wide range of starting compositions were tested,

CeIn<sub>3</sub> was always formed first by solidification [A1,A2], the remaining Pd formed Pd<sub>3</sub>In<sub>7</sub>. Based on the differential scanning calorimetry (DSC) presented in Figure 15, we showed that if the starting material (pure elements) is not heated above the melting/solidification temperature of CeIn<sub>3</sub>, the amount of CeIn<sub>3</sub> and Pd<sub>3</sub>In<sub>7</sub> is significantly reduced and more Ce<sub>n</sub>Pd<sub>m</sub>In<sub>3n+2m</sub> crystals are formed. The growth process has been summarised in Ref. A2 and A3 with suggested starting compositions to reach the proper phases. Still, the single-phase material is very difficult to prepare; one has to always perform a detailed sample characterisation to exclude or evaluate the amount of impurities. As summarised in Table 2, all Pd- and Pt- based compounds, except CePt<sub>2</sub>In<sub>7</sub>, have almost identical basal-plane lattice parameters with CeIn<sub>3</sub>. This is probably the reason why these materials crystalize at the same temperatures and it is difficult to obtain a single-phase sample.



FFigure 15 a) Calorimetric studies started from pure elements placed in an alumina crucible. In a) the system was heated only to  $750^{\circ}$ C and in b) up to  $950^{\circ}$ C. When the system is heated to the higher temperature CeIn<sub>3</sub> and Pd<sub>3</sub>In<sub>7</sub> are formed, reducing the yield of the Ce<sub>n</sub>T<sub>m</sub>In<sub>3n+2m</sub> phases and the phases grow on top of the CeIn<sub>3</sub> crystals.

There was often discussion about the existence of **CePdIn**<sub>5</sub>. We detected a phase with composition close to CePdIn<sub>5</sub> in several single crystals by EDX analysis. Its presence is rather rare. We have not succeeded in isolating it for further studies. A sample containing CePdIn<sub>5</sub> is presented in Figure 16. CePdIn<sub>5</sub> is not detectable from the sample surface – many Ce<sub>2</sub>PdIn<sub>8</sub> samples need to be cut/broken to find the CePdIn<sub>5</sub> phase inside. Single-crystal diffraction performed on the two-phase sample resulted in the lattice parameter presented in Table 2

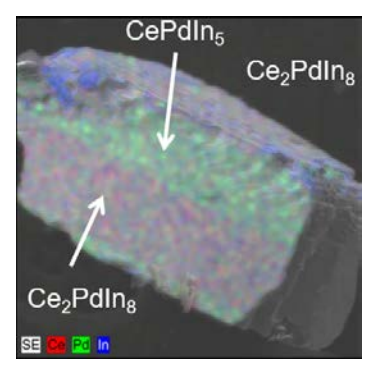


Figure 15: An SEM image of the CePdIn<sub>5</sub> – Ce<sub>2</sub>PdIn<sub>8</sub> sample. The phases grow on top of each other sharing their common ab plane.

Table 2: The lattice constants of the reported  $Ce_nT_mIn_{3n+2m}$  compounds and the lattice mismatch between their a value and a value of  $CeIn_3$ .

compounds	a (Å)	c (Å)	Mismatch (%)
CePt <sub>2</sub> In <sub>7</sub>	4.599	21.58	-1.96%
CeCoIn <sub>5</sub>	4.613	7.551	-1.65%
Ce <sub>2</sub> CoIn <sub>8</sub>	4.640	12.25	-1.06%
CeRhIn <sub>5</sub>	4.656	7.542	-0.71%
Ce <sub>2</sub> RhIn <sub>8</sub>	4.665	12.24	-0.51%
CeIrIn <sub>5</sub>	4.674	7.50	-0.32%
Ce <sub>3</sub> PdIn <sub>11</sub>	4.685	16.84	-0.09%
Ce <sub>3</sub> PtIn <sub>11</sub>	4.687	16.84	-0.03%
CeIn <sub>3</sub>	4.689		0 %
Ce <sub>2</sub> IrIn <sub>8</sub>	4.690	12.31	0.01%
Ce <sub>2</sub> PtIn <sub>8</sub>	4.690	12.15	0.02%
Ce <sub>2</sub> PdIn <sub>8</sub>	4.691	12.21	0.03%
CePdIn <sub>5</sub>	4.693	7.538	0.09%
Ce <sub>5</sub> Pd <sub>2</sub> In <sub>19</sub>	4.701	29.14	0.26%
CePt <sub>2</sub> In <sub>7</sub>	4.599	21.58	-1.96%

#### Cu-Mn-As system

Because the compound contains two rather high-vapour-pressure elements Mn and As, it requires closed crucibles or ampules for the synthesis. Fortunately, when elements form compounds, the vapour pressure drops dramatically, as demonstrated not only by the fact that there was no transfer of growth material from the growth crucible, but we could even perform DSC/thermogravimetry up to relatively high temperatures of 700 ° C with no significant loss.

We have therefore tested two other approaches: solution growth using low-melting fluxes and the Bridgman method, both in closed ampoules under a pure argon atmosphere of 0.2 bar (filled at room temperature). For solution growth, Bi and Pb fluxes were tested, with Bi leading to slightly larger crystals; only Bi-flux-grown crystals have been subject to our published work [A8, A9], and later another group also used it [166].

Crystals grown in Bi-flux: After inspecting the crystals prepared by flux growth, and measuring single crystal XRD, we found that some crystals from the same batch had the expected orthorhombic structure, while others were tetragonal. The crystal composition determined by SEM EDS analysis varied slightly from the expected 1:1:1 ratio, suggesting that the composition control is crucial for the crystal structure.

In most of the samples, there was greater variation in the Cu:Mn ratio, while the As content was closer to 33.3%. We have then varied the starting composition of the rather irreproducible

magnetic properties coming probably from spurious impurities of ferromagnetic MnAs, and the composition variation between the crystals from the same batch was up to 5%. We noticed that some crystals had the expected orthorhombic structure while other compounds were tetragonal. In Figure 1, we can see typical single crystals isolated from one growth batch. The crystals have slightly different habitus and they were selected for XRD analysis. It was found that crystal composition varies within a few %. Single-crystal XRD has shown that some crystals have an orthogonal structure, while others have a tetragonal structure. Most significantly, the composition varied between Mn and Cu content, the As content appears to be almost reproducible at around 33.3%.



Figure 16: a) SEM BSE contrast image of CuMnAs single crystals grown out of Bi flux. The residual Bi impurities are bright in contrast, and the inset shows details of the sample edge.

Bridgman method: Both stoichiometric and slightly Cu rich (2-5 at. %) the starting composition was presynthetized using the solid-state reaction reported before [78] and described in more detail in A10. The polycrystals were subsequently used to grow orthorhombic and tetragonal CuMnAs by the Bridgman method, respectively. Alumina point bottom crucibles sealed in quartz glass tubes under 0.2 atm pure Ar were used in a temperature gradient furnace; the growth temperature was 900-850°C (we determined the melting point of CuMnAs). Several experiments were performed; however, the crystals were not significantly larger than those in the original polycrystalline precursor. Furthermore, there was significant compositional variation within the grown ingots that contained both the tetragonal and orthorhombic phases.

#### NaMnAs

The synthesis of NaMnAs polycrystalline samples was reported by Bronger et al., [87]. Similarly to the growth of CuMnAs, for NaMnAs growth we tested the metallic fluxes Sn, Bi, and Pb. In this case, the Sn flux was found to be most suitable for obtaining larger plate-like crystals. The pure sodium and the crystals were handled in an argon-filled glovebox to avoid sample degradation.

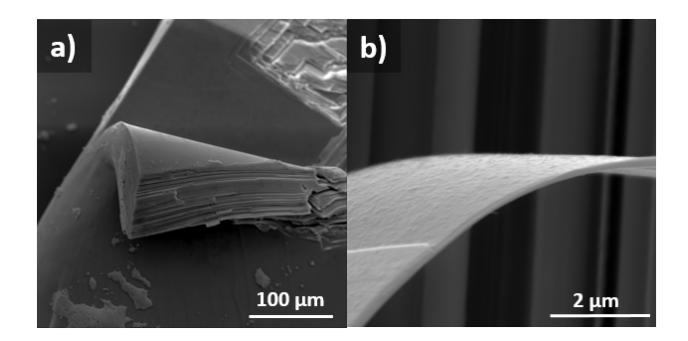


Figure 17: a) SEM images of single crystalline NaMnAs with partially cleaved surface. b) Detail of NaMnAs lamella.

The grown crystals had lateral dimensions of several millimetres with a thickness in the order of a hundred micrometres. Being sensitive to air, it was found that it decomposes to MnAs, which was also detected as a ferromagnetic impurity by magnetisation measurements. On air the materials remain with metallic lustre for few minutes then turn grey. The material is easily exfoliable using the "Scotch tape" method; see Figure 17. Such an easy exfoliation is typical for the so-called van der Waals materials. However, in NaMnAs and related systems, ionic bonds are expected [92]. Therefore, this material combines the advantage of both, being an exfoliable material and forming high quality single crystals with low mozaicity [A12].

#### MnTe

In the first works, Komatsubara et al. [99] and Zanmarchi et al. [167] reported the growth of MnTe by the Bridgman method using stoichiometric Mn: Te composition. In both groups, large MnTe ingots were grown. However, a closer analysis by Zanmarchi [168] showed the presence of cavities and grain boundaries containing MnTe<sub>2</sub>. Another Bridgman-like method was presented in the work by Mateika [168], who used a Te-rich composition (Mn: Te being in molar ratio 43.5:56.5) to avoid structural transformation of MnTe at 1026°C. This growth addressed two other problems with growing MnTe. The first was the formation of cavities in the ingot, which they significantly reduced by rotating the sample holder, and the second was the reduction of MnTe2 impurities, which they reduced by annealing the MnTe ingot in a vacuum at 900 ° C. Another work reported growth using chemical vapour transport using indium as a transport agent [169,170]. The optimal average temperature was reported to be 700°, however, for such a temperature, the phase of MnTe<sub>2</sub> impurities was present. Prereacted MnTe should be used as the feed. A study by Melo et al. [169] suggested that for CVT growth, the temperature should be above 950 °C to avoid formation of MnIn<sub>2</sub>, Aoyama et al. reported iodine CVT growth without mentioning the growth details; since their data show MnTe<sub>2</sub> is impurity-free MnTe [171,172] we expect the growth temperature would be above 741°C, below which MnTe2 can be formed. Another method, called the travelling solution method, was used by C. Reig et al. [174], who described a way to obtain impurity-free MnTe, which was grown from a Te-rich composition.

On the basis of the previous studies, and considering our experimental possibilities, we started with the Te-rich solution growth technique. Four growth methods were tested. As choice number one, Te-rich self-flux growth was used leading to high-quality plate-like single crystals with lateral dimensions of several millimetres and thickness of hundreds of micrometres with c axis being perpendicular to the plates. Figures 18 a and c show the grown crystals. The disadvantage of this growth is the limited size for some experiments and the fact that the crystals are covered by a layer of MnTe<sub>2</sub>; the cubic (111) MnTe<sub>2</sub> matches the (000l) plane of MnTe, as confirmed by XRD symmetric scan. Even after spinning at higher temperature, the phase was present on the surface. The impurity can be detected as sudden increase in magnetization below 90 K. After proper surface cleaning / polishing, no MnTe<sub>2</sub> impurity was present in the magnetisation data in Supplementary of A13 and Figure 19. Such crystals were suitable for ARPES experiments as shown in Figures 18 d and e, where the crystals prepared for cleavage and after cleave are shown.

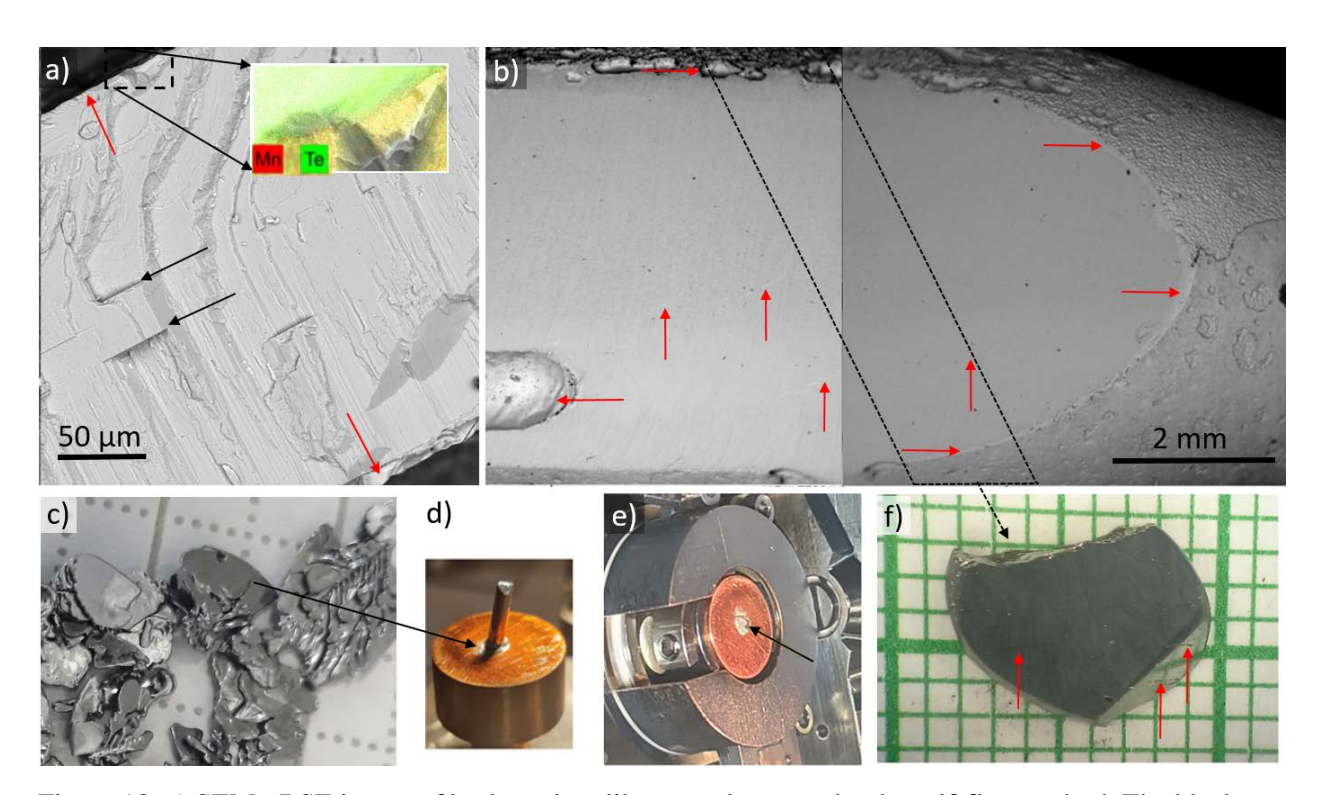


Figure 18: a) SEM - BSE image of broken plate-like crystals grown by the self-flux method. The black arrows point to the basal plane cleaves and the red arrows point to the sample surface with a thin layer of MnTe<sub>2</sub>. The inset presents an elemental map of a small surface area showing the layer of MnTe<sub>2</sub>. b) SEM BSE images (two frames) of partially polished Bridgman-grown ingot. Horizontal red arrows point to the MnTe<sub>2</sub> phase present on the surface of the ingot bubbles, and vertical arrows show the impurity planes of MnTe<sub>2</sub> within the ingot. These planes are parallel to the basal plane of MnTe. c) Optical image of flux-grown MnTe crystals (untreated surface). c) Single crystals from flux used for

ARPES: d) illustrates the MnTe sample, onto which a large pillar was glued before introduction into the UHV chamber, where it was subsequently cleaved in situ, and e) illustrates the crystal after the cleave.

However, the shape limitation was the reason for growing crystals by the Bridgman method. Both stoichiometric and Te-rich melts were used to grow MnTe. In both cases, a vertical tube furnace with temperature gradient was used. In case of the stoichiometric melt, the growth was achieved by moving the sample to the cold part of the furnace (and cooling the furnace after the growth), while for the Te-rich melt, the temperature was slowly reduced (1100-750°C, 10 days) during the growth, to cover larger temperature interval. The second approach was close to the method suggested by Reig et al., [173]. We used point bottom alumina crucibles as containers for growth. Although the final ingots contained bubbles and cavities, we obtained a good quality single crystal with a diameter of 7-8 mm and a length of 15-20 mm. The impurity phase of MnTe<sub>2</sub> was found on the surface of the bubbles and also formed plane grain boundaries along the hexagonal *ab* plane (the cubic MnTe<sub>2</sub> matches the hexagonal plane of MnTe). From the grown ingot, a disk sample with an out-of-plane a axis was prepared for a planned uSR experiment in applied fields (to be measured). The amount of MnTe<sub>2</sub> impurity can be neglected for this experiment.

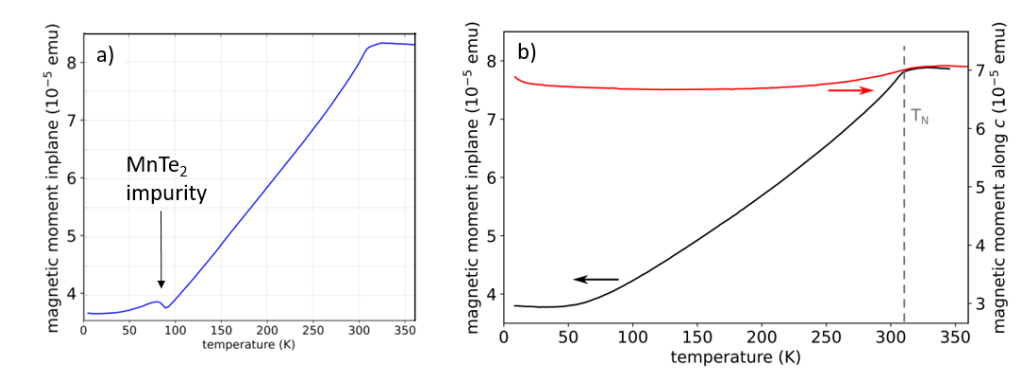


Figure 19: Magnetization data of flux-grown MnTe a) containing impurity phase and b) without MnTe<sub>2</sub> impurity, b) was taken from Ref. A13.

Other growth methods such as CVT using iodine and salt flux methods were used by other groups, and we also plan to test these methods too. When considering the temperature-composition phase diagram of MnTe, it will be important to test the transport properties with respect to different growth conditions because in semiconductors, the charge concentration and mobility strongly depend on the variation of stoichiometry and crystal defects. Finding the optimal sample preparations will be important for various future experiments.

#### $(PbS)_{1.11}VS_2$

MLCs are usually grown using the chemical vapour transport (CVT) method [141]. It was also the case of  $(PbS)_{1.11}VS_2$ . We used a modified recipe ported by Gotoh et al. [174]. Starting from pure element composition,  $(PbS)_{1.11}VS_2$  were weighted and loaded into an approximately

25 cm long fused silica tube in an Ar-filled glove box and subsequently sealed in a vacuum of 10 6 mbar.

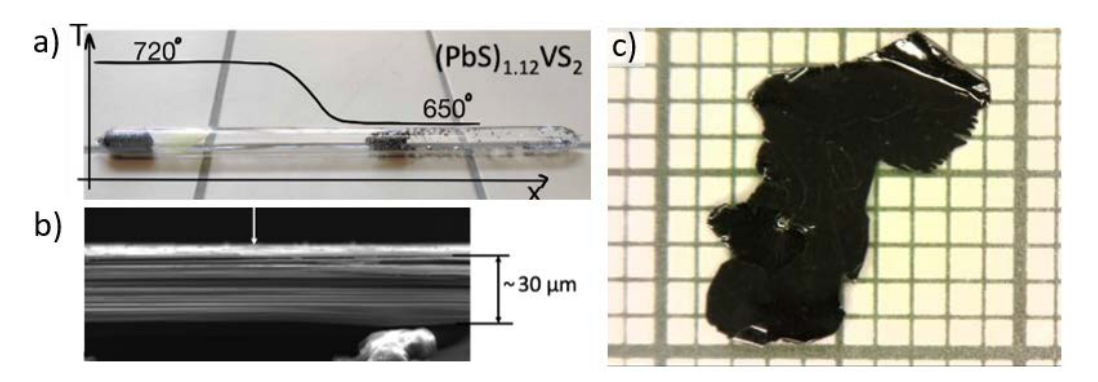


Figure 20: a) The silica tube with  $(PbS)_{1.11}VS_2$  single crystals after growth, the temperature profile is schematically depicted. b) SEM image of broken  $(PbS)_{1.11}VS_2$  crystals viewed along the basal plane direction. c) Optical image of the  $(PbS)_{1.11}VS_2$  crystal on a millimetre-scale paper.

The sample was first slowly heated in a vertical position up to 720°C and then placed in a two-zone horizontal furnace. The growth temperatures were 720°C and 650°C in the hot and cold zone, respectively, as depicted in Figure 20 a. The growth process took 1 to 6 weeks, depending on the desired size of the grown single crystals. Smaller crystals were grown for the XRD measurements. For the growth, we used about 3 grammes of materials. However, only a small part of it was transferred to single crystals. When handled in a glove box, the remaining poly crystalline material can be reused for another growth. As-grown single crystals are shiny, flat, relatively large (a couple of micrometers2), and very thin, as shown in Figures 20 b and c.

## 4.2 Microfabrication, a way to overcome sample limitations

Even after a thorough search for proper growth parameters, some materials are difficult to prepare, moreover, to obtain them in a sufficient quality and volume. One solution may be to collect tens or hundreds of crystals together; one needs to carefully attach together the sample collection (taking case about the sample orientation, when possible). Another option is to look for technique which do not require a large sample volume. A special case occurs when the volume is not the crucial parameter, but the shape. In our case, we aimed for precise determination of anisotropy in resistivity and magnetoresistance of submillimeter sample of irregular shape. Focused ion beam milling technique can be a solution for preparation of resistivity measurement devices with well-defined (microskopic) shapes of crystals. Materials whose geometrical shape would not allow for precise resistivity measurements, but also materials only available in multiphase polycrystalline samples can be isolated and subject to electrical measurements. The orientation of crystallographic axes can be determined either previously by Laue diffraction or in situ using electron back scattered diffraction (EBSD). The latter is especially useful for isolating lamellae from polycrystalline and multiphase samples.

In modern research, especially when the focus is on various delicate phenomena such as unconventional superconductivity, magnetism, crystal anisotropy, magnetoresistance, sample quality is one of the most crucial aspects. For detailed experimental studies of intrinsic properties, impurity-free single-crystalline samples are irreplaceable. However, real samples are often far from our expectations. With maximum effort, we obtain either a few tiny crystals (like in Figure 17) or crystals with intergrowths of different phases into each other as discussed, e.g. for the Ce-Pd-In and Ce-Pt-In systems. Sometimes, the problem can be solved by annealing the crystals at the proper temperature, adjusting the growth condition, or, in the case of spurious phases, repeating the growth process several times and selecting the best piece. When impurities are localised macroscopically, they can be removed by cutting or polishing; however, there are often cases where another approach would be more efficient and lead to quantitatively better results. Therefore, a microfabrication method using focused-ion beam (FIB) milling was implemented in our laboratory's measurement portfolio. Such a tool allows for the separation of well-defined single crystals with specific orientations and optimal geometry to fabricate devices with various geometries for electrical measurements or to measure single-crystal XRD.

Implementing the FIB technique for sample fabrication started in 2013/2014. Regarding our research of Ce-based heavy fermion systems, CeCoIn<sub>5</sub> was chosen as the test material. CeCoIn<sub>5</sub> is a well-known heavy fermion superconductor with a high residual resistivity ratio (RRR) and the highest ambient pressure critical temperature of 2.3 K [37] making it a good material to compare the parameters of the fabricated devices. The first devices were prepared using transfer onto the substrate as shown in Figure 19. In this case, the FIB-fabricated single-crystalline bar. However, there were principal problems with leakage currents under the transferred samples using this experimental design. The surface of the substrate under and

around the sample bar was contaminated by sputtered gas injection and by material during needle removal. As a consequence, there were significant current leakages through the substrates. As a consequence, the measurement of the test material CeCoIn<sub>5</sub> did not reach zero resistance below  $T_c = 2.1$  K, although the transition was visible at the correct temperature as presented in Figure 21 a) (see also the bachelor thesis of J. Volný [175] for more details).

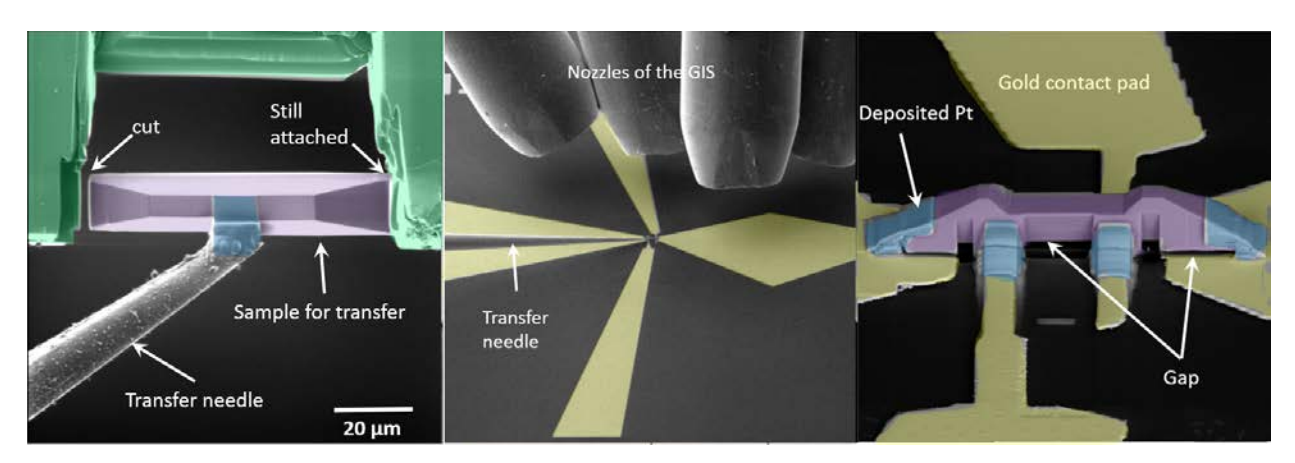


Figure 21. The sequence of sample preparation (CeCoIn5 single crystal), SEM images in false colours: Purple = sample, blue = Pt-rich solid, yellow = gold contact pads, green = the original bulk crystal: a) attaching transfer needle to the crystal by GIS platinum deposition b) from the GIS nozzles, the platinum precursors (Ch<sub>3</sub>)3Pt(CpCH<sub>3</sub>) is spread onto the sample and is decomposed by the ion beam (or electron beam) where the nonvolatile Pt-rich solid adsorbs locally at the illuminated area. c) The fabricated device. The gap below the sample is unavoidable by this type of transfer and is a source of leakage currents; the material is deposited underneath the sample during the Pt-deposition and during the removal of the transfer needle and cannot be removed by FIB anymore.

Soon after that, we decided to adopt the procedure using ex situ transfer introduced by Phillip Moll et al. in 2015 [176] and visited his group at the Map Planck Institute for Chemical Physics of Solids in Dresden to learn the alternative transfer and fabrication method. He also confirmed that in situ transfer was not a promising direction because of leakage currents and other technical difficulties (personal communication). Ex situ transfer of FIB fabricated lamella is described in Figure 8 (Here, the transfer of CuMnAs is presented because it was better documented. However, our first devices were CeCoIn<sub>5</sub> and Ce<sub>2</sub>PdIn<sub>8</sub>).

We have adopted the technique developed by P. Moll [81,176]) to prepare microstructured samples for electrical resistivity measurements. This technique is based on fabrication of single crystalline lamella with lateral dimension of tens of micrometres and thickness of 1-4 um using Scanning Electron Microscope with additional Focused Ion Beam source, so called dual-beam system. The lamellae are then ex situ transferred on a substrate, then further structured to the desired shape together with electrical leads. The procedure may slightly vary; however, the exsitu transfer is a crucial step which allows for good sample attachment on the substrate. Trying to transfer the lamella in situ like using the needle nano-manipulator leads not only to high risk

of sample losses but also, most importantly, to leakage currents that distort the resistivity measurements (j.Volný, Bc thesis [175], Moll-private communication).

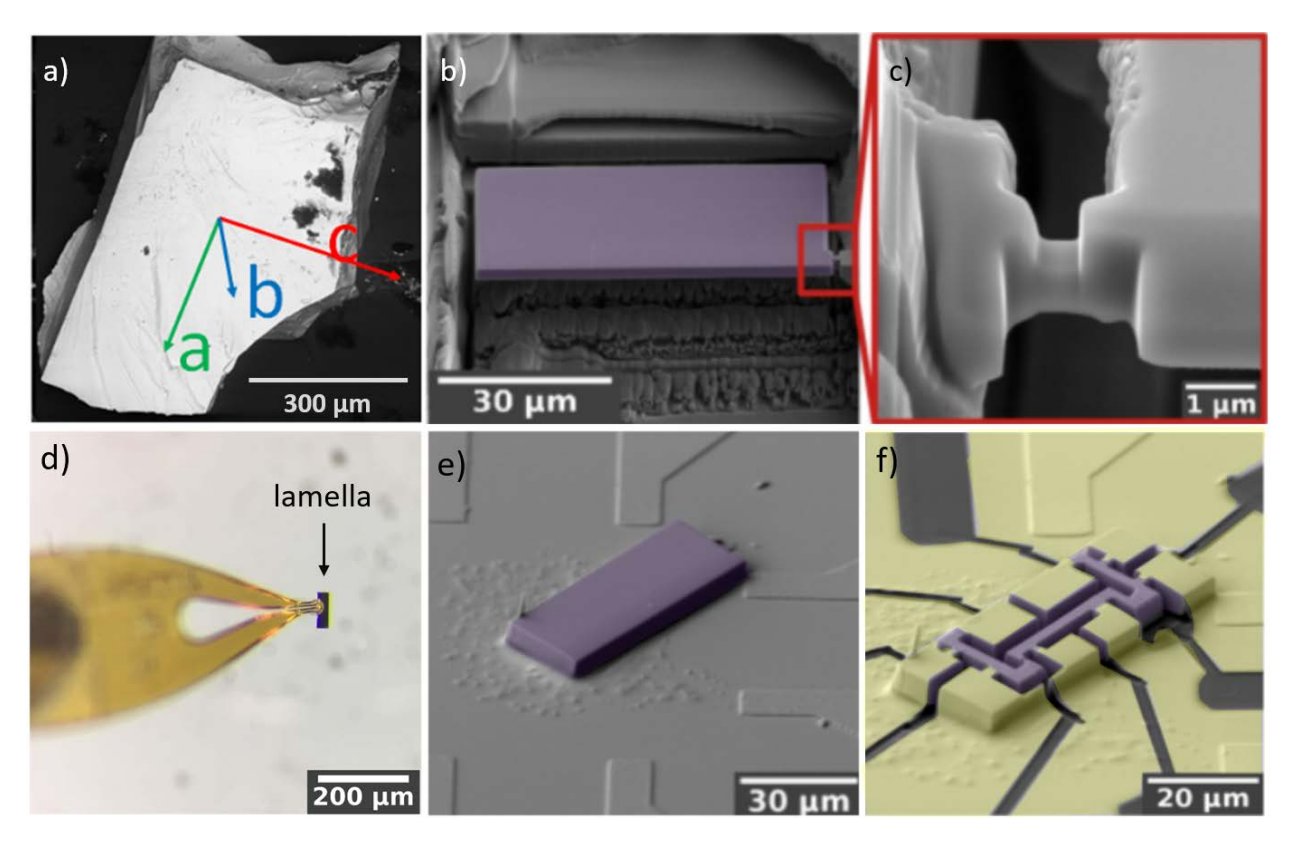


Figure 22: Device fabrication of CuMnAs single crystal. False colours: purple = lamella, yellow = gold. a) Pre-orientated single crystal, b) FIB fabricated lamella still attached to the original crystal by a bridge; this is in detail in c). d) After the lamella by a Kapton needle (ex situ under an optical microscope), the lamella stays attached to the needle due to electrostatic forces. e) SEM image of the lamella attached to the substrate (gold was evaporated on the whole area around the lamella). f) Using the FIB, the final form of the device was made. Adapted from the diploma thesis of J. Volný [82].

In Figure 20 we show the case where the lamella can be hold on the substrate just by electrostatic force. For electrical leads fabrication, gold was evaporated on the lamella and surrounding area. Subsequently, the gold was removed and the tranches were made by the FIB to form the desired structure. In Figure 21 b) and c) we present two other modifications. The first is to add GIS-assisted Pt-deposition of the contacts (in this case, there is no risk that the material would be deposited under the sample) and another option is to transfer the lamella on a droplet of glue. We did not find any significant differences in the transport properties between these devices. As can be seen in Figure 21 b) and c), the CeCoIn<sub>5</sub> sample reached similar resistance values and reached zero resistance below the critical temperature.

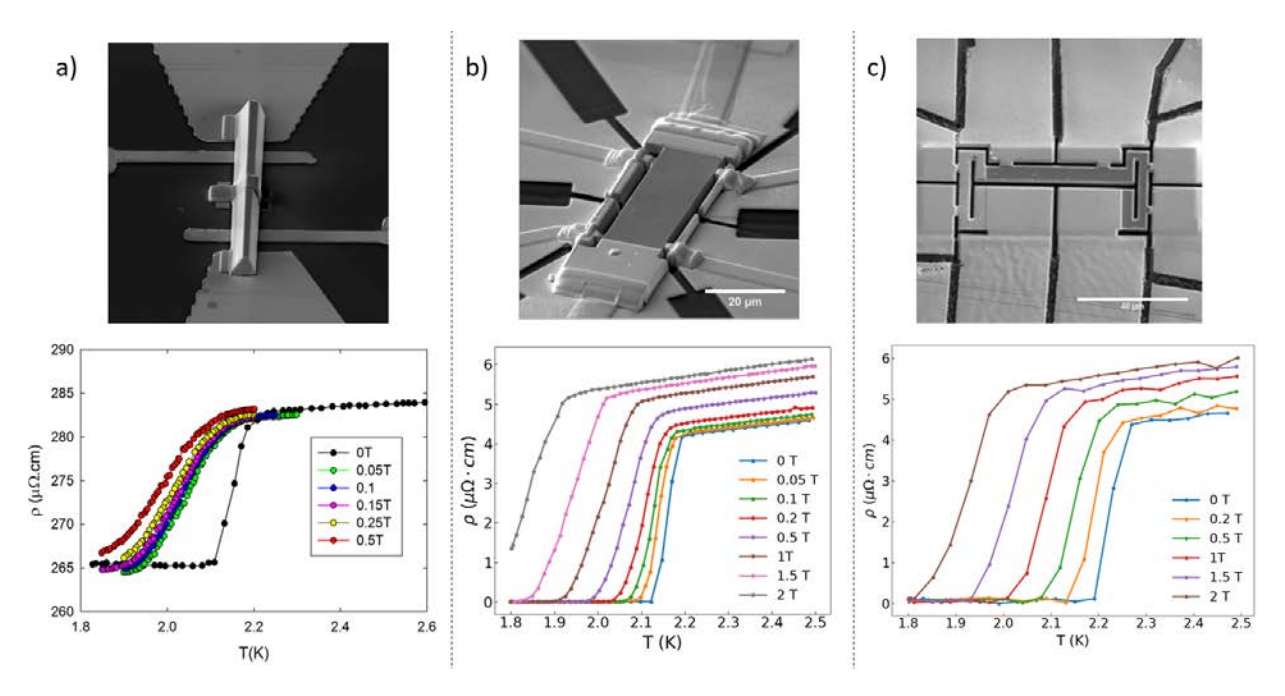


Figure 23: Comparison of the low-temperature electrical resistivity between CeCoIn<sub>5</sub> devices prepared by a) the in situ transfer method, b) the ex situ transfer method with a crystal placed on the clean substrate and a combination of evaporated gold + GIS deposited Pt contacts, and c) the in situ transfer method with crystals placed on an epoxy droplet and evaporated gold contacts. With the permission of J. Volný.

Here, we have shown both the in situ and ex situ transfer procedures. Technically, in situ transfer is much more difficult than ex situ transfer, and to the best of our knowledge, only ex situ transfer is used for the preparation of charge-/spin-transport-related devices. As mentioned above, the reason comes from the fact that it is technically almost impossible to attach the lamella to the substrate without a gap between the sample and the substrate, which is always a source of undefined leakage currents. The sample fabrication for basic transport measurements using ex situ transfer is, on the other hand, not very difficult. The whole process of making one sample takes one or two working days, depending on the methods of putting the electrical leads (GIS-deposited Pt, evaporated/sputtered gold). For the beginner, the most important part is overcoming the mental block leaving the relatively large lamella hanging on a tiny bridge (it must be narrower than 1 um for most of the materials). When leaving the bridge thicker, it tends to bend (and subsequently jump) rather than gently braking and sticking to the transfer needle electrostatically. There are, however, more challenging structures that can be used. Within about the last 10 years, FIB assisted fabrication has been developed into a powerful tool for studying quantum properties of matter by fabrications of various sophisticated devices with submicrometer resolution or assisting to well defined cleavages for spectroscopy measurements, such as ARPES, as e.g. in [81,177–179] or in the recent Roadmap for focused ion beam technologies [180].

## 4.3 Summary

This chapter has shown the variability of methods that can be used for the growth of materials. We demonstrated how proper characterisation of the growth products or studies of the crystallisation by calorimetry can help to improve the growth conditions and lead to improvements of sample quality. A special section was devoted to cope with limited crystals dimension, showing that even with tiny crystals, quantitative measurements of resistivity can be conducted.

## **5** General Summary

In this work, I introduced my work in materials research and demonstrated the importance and flexibility of crystal growth techniques for following research trends. Summarises results from 17 articles from different fields of my past and current interests. All of them were topical at the time they were published (or will be published; three attached articles are still in the review process). We can see that with the variety of available crystal growth techniques, we have the flexibility to react to current research trends.

In the case of the Ce<sub>n</sub>T<sub>m</sub>In<sub>n+2m</sub>, we prepared non-trivially grown single crystals of Ce2PdIn8 just a few months after the first article about the existence of polycrystalline material was reported. Subsequently, we introduced growth procedures for the whole series of compounds contacting Pd and Pt at the transition metal place, still being. As such, we could conduct pioneering research reporting the unique properties of Ce<sub>3</sub>PdIn<sub>11</sub> and Ce<sub>3</sub>PtIn<sub>11</sub>.

The growth materials for antiferromagnetic spintronics have followed the theoretical predictions in such a way that our samples were at the start of the success of CuMnAs thin-film research, which led to the realisation of antiferromagnetic switching and the proof-of-concept fabrications of functional memory devices. Recent theoretical work on so-called altermagnets would not get such great publicity without being experimentally confirmed. Here, the bulk MnTe crystals "beat" the high-quality epitaxial films due to the possibility of providing a quality and single-domain cleaved surface. In this case, the growth of MnTe was straightforward, and the crystals with basic characterisation were available within two weeks, demonstrating the flexibility we sometimes have.

Special attention should be paid to the research of MLCs, namely (PbS)<sub>1.11</sub>VS<sub>2</sub>, where we were the first group to report sliding ferroelectricity created in a material by natural twinning. Unlike in manually stacked multilayers, the twinned interfaces are atomically clean. Considering the fact that some MLCs are also the misfit layer compounds, should attract much attention in studies of 2D multiferroicity.

The seemingly different field of MLCs or van der Waals materials, in general, connects with the previous topics surprisingly well, not only because of the fact that some MLCs are superconducting. The symmetry breaking induced by twisting is of high interest in theoretical predictions of altermagnetism in van der Waals materials. Finding materials with proper magnetic order and a tendency for twinning may be a route for the exploration of exotic magnetic states.

## List of original papers

A1. Comment on "Emergence of a Superconducting State from an Antiferromagnetic Phase in Single Crystals of the Heavy Fermion Compound Ce<sub>2</sub>PdIn<sub>8</sub>

K. Uhlířová, J. Prokleška, V. Sechovský,

Phys. Rev. Lett. 104 (2010) 059701.

https://doi.org/10.1103/PhysRevLett.104.059701.

# A2. Solution growth of Ce-Pd-In single crystals: Characterization of the heavy-fermion superconductor Ce<sub>2</sub>PdIn<sub>8</sub>

K. Uhlířová, J. Prokleška, V. Sechovský, S. Daniš, <u>K. Uhlířová</u>, J. Prokleška, V. Sechovský, S. Daniš,

Intermetallics 18 (2010) 2025–2029. https://doi.org/10.1016/j.intermet.2010.03.017.

## A3. Single crystal study of the layered heavy fermion compounds Ce<sub>2</sub>PdIn<sub>8</sub>, Ce<sub>3</sub>PdIn<sub>11</sub>, Ce<sub>2</sub>PtIn<sub>8</sub> and Ce<sub>3</sub>PtIn<sub>11</sub>

M. Kratochvílová, M. Dusek, <u>K. Uhlířová</u>, A. Rudajevova, J. Prokleška, B. Vondráčková, J. Custers, V. Sechovský,

J. Cryst. Growth. 397 (2014) 47–52. https://doi.org/10.1016/j.jcrysgro.2014.04.008.

# A4. Coexistence of Antiferromagnetism and Superconductivity in Heavy Fermion Cerium Compound Ce<sub>3</sub>PdIn<sub>11</sub>

M. Kratochvílová, J. Prokleška, <u>K. Uhlířová</u>, V. Tkáč, M. Dušek, V. Sechovský, J. Custers,

Sci. Rep. 5 (2015) 15904 <a href="https://doi.org/10.1038/srep15904">https://doi.org/10.1038/srep15904</a>.

# A5. Magnetism, superconductivity, and quantum criticality in the multisite cerium heavy-fermion compound Ce<sub>3</sub>PtIn<sub>11</sub>

J. Prokleška, M. Kratochvílová, <u>K. Uhlířová</u>, V. Sechovský, J. Custers, *Phys. Rev. B* 92 (2015) 161114. <a href="https://doi.org/10.1103/PhysRevB.92.161114">https://doi.org/10.1103/PhysRevB.92.161114</a>.

# A6. <sup>115</sup>In NQR study with evidence for two magnetic quantum critical points in dual Ce site superconductor Ce<sub>3</sub>PtIn<sub>11</sub>.

S. Kambe, H. Sakai, Y. Tokunaga, R.E. Walstedt, M. Kratochvílová, <u>K. Uhlířová</u>, J. Custers,

Phys. Rev. B. 101 (2020) 081103. https://doi.org/10.1103/PhysRevB.101.081103.

### A7. Room-temperature antiferromagnetism in CuMnAs

F. MácA, J. Masek, O. Stelmakhovych, X. Martí, H. Reichlová, <u>K. Uhlířová</u>, P. Beran, P. Wadley, V. Novák, T. Jungwirth, J. Mašek, O. Stelmakhovych, X. Martí, H. Reichlová, K. Uhlířová, P. Beran, P. Wadley, V. Novák, T. Jungwirth, , *J. Magn. Magn. Mater*. 324 (2012) 1606–1612. https://doi.org/10.1016/j.jmmm.2011.12.017.

### A8. Synthesis and single crystal study of CuMn<sub>3</sub>As<sub>2</sub> and Cu<sub>2</sub>Mn<sub>4</sub>As<sub>3</sub>,

K. Uhlířová, R. Tarasenko, F.J. Martínez-Casado, B. Vondráčková, Z. Matěj, *J. Alloys Compd.* 650 (2015) 224–227. https://doi.org/10.1016/j.jallcom.2015.07.208.

### A9. Band structure of CuMnAs probed by optical and photoemission spectroscopy

M. Veis, J. Minár, G. Steciuk, L. Palatinus, C. Rinaldi, M. Cantoni, D. Kriegner, K.K.K. Tikuišis, J. Hamrle, M. Zahradník, R. Antoš, J. Železný, L. Šmejkal, X. Marti, P. Wadley, R.P.P. Campion, C. Frontera, <u>K. Uhlířová</u>, T. Duchoň, P. Kužel, V. Novák, T. Jungwirth, K. Výborný,

Phys. Rev. B. 97 (2018) 125109. https://doi.org/10.1103/PhysRevB.97.125109.

# A10. The stability and physical properties of the tetragonal phase of bulk CuMnAs antiferromagnets

K. Uhlířová, E. Duverger-Nédellec, R.H. Colman, J. Volný, B. Vondráčková, K. Carva,

J. Alloys Compd. 771 (2019) 680–685. https://doi.org/10.1016/j.jallcom.2018.08.199.

### A11. Electrical transport properties of bulk tetragonal CuMnAs

J. Volný, D. Wagenknecht, J. Železný, P. Harcuba, E. Duverger-Nedellec, R.H. Colman, J. Kudrnovský, I. Turek, <u>K. Uhlířová</u>, K. Výborný, *Phys. Rev. Mater.* 4 (2020) 064403.

https://doi.org/10.1103/PhysRevMaterials.4.064403.

# A12. Single-crystal studies and electronic structure investigation of the room-temperature semiconductor NaMnAs

J. Volný, K. Charvátová, M. Veis, V. Holý, M. Vondráček, J. Honolka, E. Duverger-Nédellec, J. Schusser, S.W. D'Souza, J. Minár, J.M. Pientka, A. Marmodoro, K. Výborný, K. Uhlířová,

Phys. Rev. B. 105 (2022) 125204. https://doi.org/10.1103/PhysRevB.105.125204.

#### A13. Altermagnetic lifting of Kramers spin degeneracy

J. Krempaský, L. Šmejkal, S.W. D'Souza, M. Hajlaoui, G. Springholz, K. Uhlířová,

F. Alarab, P.C. Constantinou, V. Strocov, D. Usanov, W.R. Pudelko, R. González-

Hernández, A. Birk Hellenes, Z. Jansa, H. Reichlová, Z. Šobáň, R.D. Gonzalez Betancourt, P. Wadley, J. Sinova, D. Kriegner, J. Minár, J.H. Dil, T. Jungwirth, *Nature* 626 (2024) 517–522. https://doi.org/10.1038/s41586-023-06907-7.

### A14. Sliding ferroelectricity in a bulk misfit layer compound (PbS)<sub>1.11</sub>VS<sub>2</sub>,

C. Antunes Corrêa, J. Volný, K. Tetalová, <u>K. Uhlířová</u>, V. Petříček, M.Vondráček, J. Honolka, and T. Verhagen;

under review in Phys. Rev. Lett., preprint: arXiv:2306.14446

#### A15. Mapping sliding ferroelectricity in bulk (PbS)<sub>1.11</sub>VS<sub>2</sub> crystals:

C. Antunes Corrêa, J. Volný, <u>K. Uhlířová</u>, T. Verhagen, *Phys. Status Solidi – Rapid Res. Lett.* 18 (2024) 2400189, <a href="https://doi.org/10.1002/pssr.202400189">https://doi.org/10.1002/pssr.202400189</a>

### A16. Electron beam patterning in sliding-ferroelectric compound (PbS)<sub>1.11</sub>VS<sub>2</sub>:

J. Volný, K. Tetalová, C. Antunes Corrêa, T. Verhagen, and <u>K. Uhlířová</u>, *under review in Phys. Rev. Applied* 

### A17. Sliding ferroelectric moiré domains for carbon nanoparticle catalysis

J. Vaníčková, <u>K. Uhlířová</u>, J. Volný, T. Verhagen, submited to *NanoLetters* 

## References

- [1] B. D. White, J. D. Thompson, and M. B. Maple, Phys. C Supercond. Its Appl. **514**, 246 (2015).
- [2] E. Bauer, in *Encycl. Mater. Sci. Technol.*, edited by K. H. J. Buschow, W. C. Robert, C. F. Merton, print Bernard Ilschner, J. K. Edward, M. Subhash, and updates Patrick Veyssi�re (Elsevier, Oxford, 2001), pp. 4372–4381.
- [3] P. Fulde, J. Keller, and G. Zwicknagl, in *Solid State Phys. Adv. Res. Appl.*, edited by H. E. and D. Turnbull (Academic Press, 1988), pp. 1–150.
- [4] T. Manfred Sigrist and Kazuo Ueda Institute of Materials Science. University of Tsukuba, Rev. Mod. Phys. **63**, 239 (1991).
- [5] E. Bauer, G. Hilscher, H. Michor, C. Paul, E. W. Scheidt, A. Gribanov, Y. Seropegin, H. Noël, M. Sigrist, and P. Rogl, Phys. Rev. Lett. **92**, 4 (2004).
- [6] K. Andres, J. E. Graebner, and H. R. Ott, Phys. Rev. Lett. **35**, 1779 (1975).
- [7] F. Steglich, J. Aarts, C. D. Bredl, W. Lieke, D. Meschede, W. Franz, and H. Schäfer, Phys. Rev. Lett. 43, 1892 (1979).
- [8] H. R. Ott, H. Rudigier, Z. Fisk, and J. L. Smith, Phys. Rev. Lett. **50**, 1595 (1983).
- [9] H. R. Ott, H. Rudigier, T. M. Rice, K. Ueda, Z. Fisk, and J. L. Smith, Phys. Rev. Lett. **52**, 1915 (1984).
- [10] R. A. Fisher, S. Kim, B. F. Woodfield, N. E. Phillips, L. Taillefer, K. Hasselbach, J. Flouquet, A. L. Giorgi, and J. L. Smith, Phys. Rev. Lett. **62**, 1411 (1989).
- [11] G. R. Stewart, Z. Fisk, J. O. Willis, and J. L. Smith, Phys. Rev. Lett. **52**, 679 (1984).
- [12] C. Pfleiderer, Rev. Mod. Phys. **81**, 1551 (2009).
- [13] S. Paschen and Q. Si, Nat. Rev. Phys. **3**, 9 (2021).
- [14] P. Monthoux, D. Pines, and G. G. Lonzarich, Nature **450**, 1177 (2007).
- [15] M. R. Norman, Science (80-.). **332**, 196 (2011).
- [16] Y. Dalichaouch, M. C. Deandrade, and M. B. Maple, Phys. Rev. B 46, 8671 (1992).
- [17] R. Joynt and L. Taillefer, Rev. Mod. Phys. **74**, 235 (2002).
- [18] P. Monthoux and G. G. Lonzarich, Phys. Rev. B **69**, 64517 (2004).
- [19] H. V. Löhneysen, A. Rosch, M. Vojta, and P. Wölfle, Rev. Mod. Phys. **79**, 1015 (2007).
- [20] A. Schofieid, Phys. World **16**, 23 (2003).
- [21] P. G. Pagliuso, N. J. Curro, N. O. Moreno, M. F. Hundley, J. D. Thompson, J. L. Sarrao, and Z. Fisk, Phys. B Condens. Matter **320**, 370 (2002).
- [22] H. Hegger, C. Petrovic, E. G. Moshopoulou, M. F. Hundley, J. L. Sarrao, Z. Fisk, and J. D. Thompson, Phys. Rev. Lett. **84**, 4986 (2000).

- [23] K. H. J. Buschow, in *Encycl. Mater. Sci. Technol.*, edited by K. H. J. Buschow, W. C. Robert, C. F. Merton, print Bernard Ilschner, J. K. Edward, M. Subhash, and updates Patrick Veyssi re (Elsevier, Oxford, 2001), pp. 4813–4817.
- [24] G. Knebel, D. Braithwaite, P. C. Canfield, G. Lapertot, and J. Flouquet, Phys. Rev. B Condens. Matter Mater. Phys. **65**, 244251 (2002).
- [25] I. R. Walker, F. M. Grosche, D. M. Freye, and G. G. Lonzarich, Phys. C Supercond. Its Appl. **282–287**, 303 (1997).
- [26] C. Petrovic, R. Movshovich, M. Jaime, P. G. Pagliuso, M. F. Hundley, J. L. Sarrao, Z. Fisk, and J. D. Thompson, Europhys. Lett. **53**, 354 (2001).
- [27] M. P. Allan, F. Massee, D. K. Morr, J. Van Dyke, A. W. Rost, A. P. Mackenzie, C. Petrovic, and J. C. Davis, Nat. Phys. 9, 468 (2013).
- [28] B. B. Zhou, S. Misra, E. H. Da Silva Neto, P. Aynajian, R. E. Baumbach, J. D. Thompson, E. D. Bauer, and A. Yazdani, Nat. Phys. 9, 474 (2013).
- [29] K. Izawa, H. Yamaguchi, Y. Matsuda, H. Shishido, R. Settai, and Y. Onuki, Phys. Rev. Lett. 87, 57002 (2001).
- [30] M. Kenzelmann, T. Strässle, C. Niedermayer, M. Sigrist, B. Padmanabhan, M. Zolliker, A. D. Bianchi, R. Movshovich, E. D. Bauer, J. L. Sarrao, and J. D. Thompson, Science (80-.). **321**, 1652 (2008).
- [31] M. Kenzelmann, S. Gerber, N. Egetenmeyer, J. L. Gavilano, T. Strässle, A. D. Bianchi, E. Ressouche, R. Movshovich, E. D. Bauer, J. L. Sarrao, and J. D. Thompson, Phys. Rev. Lett. **104**, 24 (2010).
- [32] R. Settai, H. Shishido, S. Ikeda, Y. Murakawa, M. Nakashima, D. Aoki, Y. Haga, H. Harima, and Y. Onuki, J. Phys. Condens. Matter **13**, (2001).
- [33] H. Shishido, R. Settai, S. Hashimoto, Y. Inada, and Y. Onuki, J. Magn. Magn. Mater. **272–276**, 225 (2004).
- [34] W. Bao, P. G. Pagliuso, J. L. Sarrao, J. D. Thompson, Z. Fisk, J. W. Lynn, and R. W. Erwin, Phys. Rev. B Condens. Matter Mater. Phys. **62**, R14621 (2000).
- [35] G. Knebel, J. Buhot, D. Aoki, G. Lapertot, S. Raymond, E. Ressouche, and J. Flouquet, J. Phys. Soc. Japan **80**, 1 (2011).
- [36] T. Park, F. Ronning, H. Q. Yuan, M. B. Salamon, R. Movshovich, J. L. Sarrao, and J. D. Thompson, Nature **440**, 65 (2006).
- [37] R. Movshovich, M. Jaime, J. D. Thompson, C. Petrovic, Z. Fisk, P. G. Pagliuso, and J. L. Sarrao, Phys. Rev. Lett. **86**, 5152 (2001).
- [38] G. Chen, S. Ohara, M. Hedo, Y. Uwatoko, K. Saito, M. Sorai, and I. Sakamoto, J. Phys. Soc. Japan **71**, 2836 (2002).
- [39] M. Hedo, N. Kurita, Y. Uwatoko, G. Chen, S. Ohara, and I. Sakamoto, J. Magn. Magn. Mater. **272**–**276**, 146 (2004).
- [40] G. Chen, S. Ohara, M. Hedo, Y. Uwatoko, and I. Sakamoto, J. Phys. Condens. Matter 15, S2175 (2003).

- [41] M. Nicklas, V. A. Sidorov, H. A. Borges, P. G. Pagliuso, C. Petrovic, Z. Fisk, J. L. Sarrao, and J. D. Thompson, Phys. Rev. B Condens. Matter Mater. Phys. 67, 205061 (2003).
- [42] E. G. Moshopoulou, R. M. Ibberson, J. L. Sarrao, J. D. Thompson, and Z. Fisk, Acta Crystallogr. Sect. B Struct. Sci. **62**, 173 (2006).
- [43] G. D. Morris, R. H. Heffner, N. O. Moreno, P. G. Pagliuso, J. L. Sarrao, S. R. Dunsiger, G. J. Nieuwenhuys, D. E. MacLaughlin, and O. O. Bernal, Phys. Rev. B Condens. Matter Mater. Phys. 69, (2004).
- [44] R. H. Heffner, G. D. Morris, E. D. Bauer, J. L. Sarrao, J. D. Thompson, D. E. MacLaughlin, and L. Shu, Phys. B Condens. Matter **374–375**, 184 (2006).
- [45] R. T. Macaluso, J. L. Sarrao, N. O. Moreno, P. G. Pagliuso, J. D. Thompson, F. R. Fronczek, M. F. Hundley, A. Malinowski, and J. Y. Chan, Chem. Mater. **15**, 1394 (2003).
- [46] H. Shishido, R. Settai, H. Harima, and Y. Onuki, Phys. B Condens. Matter **378–380**, 92 (2006).
- [47] Y. Onuki, S. Ikeda, H. Yamagami, A. Galatanu, Y. Haga, T. D. Matsuda, E. Yamamoto, and R. Settai, Phys. B Condens. Matter **378–380**, 972 (2006).
- [48] T. Ueda, H. Shishido, S. Hashimoto, T. Okubo, M. Yamada, Y. Inada, R. Settai, H. Harima, A. Galatanu, E. Yamamoto, N. Nakamura, K. Sugiyama, T. Takeuchi, K. Kindo, T. Namiki, Y. Aoki, H. Sato, and Y. Onuki, J. Phys. Soc. Japan 73, 649 (2004).
- [49] A. Schenck, F. N. Gygax, T. Ueda, and Y. Onuki, Phys. Rev. B Condens. Matter Mater. Phys. **70**, (2004).
- [50] N. D. Mathur, F. M. Grosche, S. R. Julian, I. R. Walker, D. M. Freye, R. K. W. Haselwimmer, and G. G. Lonzarich, Nature **394**, 39 (1998).
- [51] P. Monthoux, J. Phys. Condens. Matter **15**, (2003).
- [52] P. Monthoux and G. G. Lonzarich, Phys. Rev. B **59**, 14598 (1999).
- [53] S. N. Nesterenko, A. I. Tursina, D. V. Shtepa, H. Noel, and Y. D. Seropegin, J. Alloys Compd. 442, 93 (2007).
- [54] D. Kaczorowski, A. Pikul, B. Belan, L. Sojka, and Y. Kalychak, Phys. B Condens. Matter **404**, 2975 (2009).
- [55] D. Kaczorowski, A. P. Pikul, D. Gnida, and V. H. Tran, Phys. Rev. Lett. **103**, 27003 (2009).
- [56] K. Uhlířová, J. Prokleška, and V. Sechovský, Phys. Rev. Lett. **104**, 059701 (2010).
- [57] D. Kaczorowski, A. P. Pikul, D. Gnida, and V. H. Tran, Phys. Rev. Lett. **104**, 59702 (2010).
- [58] K. Uhlířová, J. Prokleška, V. Sechovský, S. Daniš, K. Uhlírová, J. Prokleska, V. Sechovsky, and S. Danis, INTERMETALLICS **18**, 2025 (2010).
- [59] A. Tursina, S. Nesterenko, Y. Seropegin, H. Noël, and D. Kaczorowski, J. Solid State Chem. **200**, 7 (2013).

- [60] Z. M. Kurenbaeva, E. V. Murashova, Y. D. Seropegin, H. Noël, and A. I. Tursina, Intermetallics **16**, 979 (2008).
- [61] E. D. Bauer, N. Kurita, V. A. Sidorov, F. Ronning, R. Movshovich, J. D. Thompson, B. E.D., K. N., S. V.A., R. F., R. Movshovich, and T. J.D., *Tu-HT4-01 Complex Magnetic Order in CePt2In7* (2009).
- [62] T. Klimczuk, O. Walter, L. Müchler, J. W. Krizan, F. Kinnart, and R. J. Cava, J. Phys. Condens. Matter **26**, (2014).
- [63] D. Kaczorowski, A. P. Pikul, D. Gnida, and V. H. Tran, Phys. Rev. Lett. **103**, 027003 (2009).
- [64] D. Kaczorowski, D. Gnida, A. P. Pikul, and V. H. Tran, Solid State Commun. **150**, 411 (2010).
- [65] J. K. Dong, H. Zhang, X. Qiu, B. Y. Pan, Y. F. Dai, T. Y. Guan, S. Y. Zhou, D. Gnida, D. Kaczorowski, and S. Y. Li, Phys. Rev. X 1, (2011).
- [66] K. Götze, J. Klotz, D. Gnida, H. Harima, D. Aoki, A. Demuer, S. Elgazzar, J. Wosnitza, D. Kaczorowski, and I. Sheikin, Phys. Rev. B - Condens. Matter Mater. Phys. 92, 1 (2015).
- [67] H. Fukazawa, R. Nagashima, S. Shimatani, Y. Kohori, and D. Kaczorowski, J. Phys. Conf. Ser. **449**, 5 (2013).
- [68] J. Klotz, K. Götze, E. L. Green, A. Demuer, H. Shishido, T. Ishida, H. Harima, J. Wosnitza, and I. Sheikin, Phys. Rev. B **97**, 34 (2018).
- [69] M. Kratochvilova, M. Dusek, K. Uhlirova, A. Rudajevova, J. Prokleska, B. Vondrackova, J. Custers, and V. Sechovsky, J. Cryst. Growth **397**, 47 (2014).
- [70] H. Fukazawa, K. Kumeda, N. Shioda, Y. Lee, Y. Kohori, K. Sugimoto, D. Das, J. Blawat, and D. Kaczorowski, Phys. Rev. B **102**, (2020).
- [71] K. Olejník, T. Seifert, Z. Kašpar, V. Novák, P. Wadley, R. P. Campion, M. Baumgartner, P. Gambardella, P. Nemec, J. Wunderlich, J. Sinova, P. Kužel, M. Müller, T. Kampfrath, and T. Jungwirth, Sci. Adv. 4, 1 (2018).
- [72] J. Wunderlich, EP 3 474 281 A1 (n.d.).
- [73] B. G. Park, J. Wunderlich, X. Martí, V. Holý, Y. Kurosaki, M. Yamada, H. Yamamoto, A. Nishide, J. Hayakawa, H. Takahashi, A. B. Shick, and T. Jungwirth, Nat. Mater. 10, 347 (2011).
- [74] R. Duine, Nat. Mater. **10**, 344 (2011).
- [75] V. Baltz, A. Manchon, M. Tsoi, T. Moriyama, T. Ono, and Y. Tserkovnyak, Rev. Mod. Phys. **90**, 15005 (2018).
- [76] J. Železný, H. Gao, K. Výborný, J. Zemen, J. Mašek, A. Manchon, J. Wunderlich, J. Sinova, and T. Jungwirth, Phys. Rev. Lett. **113**, 157201 (2014).
- [77] P. Wadley, B. Howells, J. Železný, C. Andrews, V. Hills, R. P. Campion, V. Novák, K. Olejník, F. Maccherozzi, S. S. Dhesi, S. Y. Martin, T. Wagner, J. Wunderlich, F. Freimuth, Y. Mokrousov, J. Kuneš, J. S. Chauhan, M. J. Grzybowski, A. W. Rushforth,

- K. Edmond, B. L. Gallagher, T. Jungwirth, J. Zelezny, C. Andrews, V. Hills, R. P. Campion, V. Novák, K. Olejník, F. Maccherozzi, S. S. Dhesi, S. Y. Martin, T. Wagner, J. Wunderlich, F. Freimuth, Y. Mokrousov, J. Kunes, J. S. Chauhan, M. J. Grzybowski, A. W. Rushforth, K. W. Edmonds, B. L. Gallagher, and T. Jungwirth, Science (80-.). **351**, 587 (2016).
- [78] J. Mündelein and H. U. Schuster, Zeitschrift Fur Naturforsch. Sect. B J. Chem. Sci. 47, 925 (1992).
- [79] P. Wadley, V. Novák, R. P. Campion, C. Rinaldi, X. Martí, H. Reichlová, J. Železný, J. Gazquez, M. A. Roldan, M. Varela, D. Khalyavin, S. Langridge, D. Kriegner, F. MácA, J. Mašek, R. Bertacco, V. Holý, A. W. Rushforth, K. W. Edmonds, B. L. Gallagher, C. T. Foxon, J. Wunderlich, and T. Jungwirth, Nat. Commun. 4, 2322 (2013).
- [80] Z. Kašpar, M. Surýnek, J. Zubáč, F. Krizek, V. Novák, R. P. Campion, M. S. Wörnle, P. Gambardella, X. Marti, P. Němec, K. W. Edmonds, S. Reimers, O. J. Amin, F. Maccherozzi, S. S. Dhesi, P. Wadley, J. Wunderlich, K. Olejník, and T. Jungwirth, Nat. Electron. 4, 30 (2021).
- [81] P. J. W. Moll, Annu. Rev. Condens. Matter Phys. 9, 147 (2018).
- [82] J. Volný, Electrotransport Properties of CuMnAs Single Crystals, Charles University, 2021.
- [83] M. H. Karigerasi, K. Kang, A. Ramanathan, D. L. Gray, M. D. Frontzek, H. Cao, A. Schleife, and D. P. Shoemaker, Phys. Rev. Mater. **3**, 1 (2019).
- [84] P. Wadley, V. Hills, M. R. Shahedkhah, K. W. Edmonds, R. P. Campion, V. Novák, B. Ouladdiaf, D. Khalyavin, S. Langridge, V. Saidl, P. Nemec, A. W. Rushforth, B. L. Gallagher, S. S. Dhesi, F. MacCherozzi, J. Železný, and T. Jungwirth, Sci. Rep. 5, 17079 (2015).
- [85] S. Reimers, D. Kriegner, O. Gomonay, D. Carbone, F. Krizek, V. Novák, R. P. Campion, F. Maccherozzi, A. Björling, O. J. Amin, L. X. Barton, S. F. Poole, K. A. Omari, J. Michalička, O. Man, J. Sinova, T. Jungwirth, P. Wadley, S. S. Dhesi, and K. W. Edmonds, Nat. Commun. 13, 1 (2022).
- [86] W. Bronger, P. Mueller, R. Hoeppner, and H. -U. Schuster, Z. Anorg. Allg. Chem. 539 **539**, 175 (1986).
- [87] R. Müller, M. Kuckel, H. U. Schuster, P. Müller, and W. Bronger, J. Alloys Compd. **176**, 167 (1991).
- [88] T. Jungwirth, V. Novák, X. Martí, M. Cukr, F. MácA, A. B. Shick, J. Mašek, P. Horodyská, P. Němec, V. Holý, J. Zemek, P. Kužel, I. Němec, B. L. Gallagher, R. P. Campion, C. T. Foxon, and J. Wunderlich, Phys. Rev. B Condens. Matter Mater. Phys. 83, 1 (2011).
- [89] V. Novák, M. Cukr, Z. Šobáň, T. Jungwirth, X. Martí, V. Holý, P. Horodyská, and P. Němec, J. Cryst. Growth **323**, 348 (2011).
- [90] J. Yang, A. Wegner, C. M. Brown, and D. Louca, Appl. Phys. Lett. 113, (2018).
- [91] W. Zhou, S. Wu, and S. Li, J. Magn. Magn. Mater. **420**, 19 (2016).

- [92] R. W. McKinney, P. Gorai, S. Manna, E. Toberer, and V. Stevanović, J. Mater. Chem. A **6**, 15828 (2018).
- [93] J. Dzian, I. Mohelský, F. Le Mardelé, J. Volný, J. Wyzula, A. Pawbake, K. Výborný, S. Tazlarů, K. Uhlířová, A. Saúl, C. Faugeras, M. Veis, and M. Orlita, Prep. (2024).
- [94] J. Qi, Z. Wu, W. Wang, K. Bao, L. Wang, J. Wu, C. Ke, Y. Xu, and Q. He, Int. J. Extrem. Manuf. 5, (2023).
- [95] S. Son, Y. J. Shin, K. Zhang, J. Shin, S. Lee, H. Idzuchi, M. J. Coak, H. Kim, J. Kim, J. H. Kim, M. Kim, D. Kim, P. Kim, and J. G. Park, 2D Mater. 7, (2020).
- [96] D. Chiba, M. Sawicki, Y. Nishitani, Y. Nakatani, F. Matsukura, and H. Ohno, Nature 455, 515 (2008).
- [97] L. Šmejkal, J. Sinova, and T. Jungwirth, Phys. Rev. X 12, 040501 (2022).
- [98] L. Šmejkal, J. Sinova, and T. Jungwirth, Phys. Rev. X 12, 031042 (2022).
- [99] T. Komatsubara, M. Murakami, and E. Hirahara, J. Phys. Soc. Japan 18, 356 (1963).
- [100] T. Jungwirth, X. Marti, P. Wadley, and J. Wunderlich, Nat. Nanotechnol. 11, 231 (2016).
- [101] G. Yin, J. X. Yu, Y. Liu, R. K. Lake, J. Zang, and K. L. Wang, Phys. Rev. Lett. **122**, 106602 (2019).
- [102] D. Kriegner, K. Výborný, K. Olejník, H. Reichlová, V. Novák, X. Marti, J. Gazquez, V. Saidl, P. Němec, V. V. Volobuev, G. Springholz, V. Holý, and T. Jungwirth, Nat. Commun. 7, 1 (2016).
- [103] S. Lee, S. Lee, S. Jung, J. Jung, D. Kim, Y. Lee, B. Seok, J. Kim, B. G. Park, L. Šmejkal, C. J. Kang, and C. Kim, Phys. Rev. Lett. 132, (2024).
- [104] O. J. Amin, A. D. Din, E. Golias, Y. Niu, A. Zakharov, S. C. Fromage, C. J. B. Fields, S. L. Heywood, R. B. Cousins, F. Maccherozzi, J. Krempaský, J. H. Dil, D. Kriegner, B. Kiraly, R. P. Campion, A. W. Rushforth, K. W. Edmonds, S. S. Dhesi, L. Šmejkal, T. Jungwirth, and P. Wadley, 636, (2024).
- [105] L. Bai, W. Feng, S. Liu, L. Šmejkal, Y. Mokrousov, and Y. Yao, Adv. Funct. Mater. 34, (2024).
- [106] A. Dal Din, O. J. Amin, P. Wadley, and K. W. Edmonds, Npj Spintron. 2, 1 (2024).
- [107] A. H. Castro Neto, F. Guinea, N. M. R. Peres, K. S. Novoselov, and A. K. Geim, Rev. Mod. Phys. 81, 109 (2009).
- [108] A. K. Geim and I. V. Grigorieva, Nature **499**, 419 (2013).
- [109] Y. Du, A. T. Neal, H. Zhou, and P. D. Ye, J. Phys. Condens. Matter **28**, 263002 (2016).
- [110] Z. Q. Li, E. A. Henriksen, Z. Jiang, Z. Hao, M. C. Martin, P. Kim, H. L. Stormer, and D. N. Basov, Nat. Phys. 4, 532 (2008).
- [111] K. F. Mak, J. Shan, and D. C. Ralph, Nat. Rev. Phys. 1, 646 (2019).
- [112] M. Vizner Stern, Y. Waschitz, W. Cao, I. Nevo, K. Watanabe, T. Taniguchi, E. Sela, M. Urbakh, O. Hod, and M. Ben Shalom, Science (80-.). 372, 1462 (2021).

- [113] L. Rogée, L. Wang, Y. Zhang, S. Cai, P. Wang, M. Chhowalla, W. Ji, and S. P. Lau, Science (80-.). **376**, 973 (2022).
- [114] L. Li and M. Wu, ACS Nano 11, 6382 (2017).
- [115] Y. Saito, T. Nojima, and Y. Iwasa, Nat. Rev. Mater. 2, 16094 (2016).
- [116] K. Yasuda, X. Wang, K. Watanabe, T. Taniguchi, and P. Jarillo-Herrero, Science (80-.). 372, 1458 (2021).
- [117] A. Weston, E. G. Castanon, V. Enaldiev, F. Ferreira, S. Bhattacharjee, S. Xu, H. Corte-León, Z. Wu, N. Clark, A. Summerfield, T. Hashimoto, Y. Gao, W. Wang, M. Hamer, H. Read, L. Fumagalli, A. V. Kretinin, S. J. Haigh, O. Kazakova, A. K. Geim, V. I. Fal'ko, and R. Gorbachev, Nat. Nanotechnol. 17, 390 (2022).
- [118] R. Niu, Z. Li, X. Han, Z. Qu, D. Ding, Z. Wang, Q. Liu, T. Liu, C. Han, K. Watanabe, T. Taniguchi, M. Wu, Q. Ren, X. Wang, J. Hong, J. Mao, Z. Han, K. Liu, Z. Gan, and J. Lu, Nat. Commun. 13, 6241 (2022).
- [119] J. Valasek, Phys. Rev. 17, 475 (1921).
- [120] C. Wang, L. You, D. Cobden, and J. Wang, Nat. Mater. 22, 542 (2023).
- [121] F. Liu, L. You, K. L. Seyler, X. Li, P. Yu, J. Lin, X. Wang, J. Zhou, H. Wang, H. He, S. T. Pantelides, W. Zhou, P. Sharma, X. Xu, P. M. Ajayan, J. Wang, and Z. Liu, Nat. Commun. 7, 1 (2016).
- [122] Y. Zhou, D. Wu, Y. H. Zhu, Y. J. Cho, Q. He, X. Yang, K. Herrera, Z. D. Chu, Y. Han, M. C. Downer, H. L. Peng, and K. J. Lai, NANO Lett. 17, 5508 (2017).
- [123] W. J. Ding, J. B. Zhu, Z. Wang, Y. F. Gao, D. Xiao, Y. Gu, Z. Y. Zhang, and W. G. Zhu, Nat. Commun. **8**, (2017).
- [124] X. Wang, K. Yasuda, Y. Zhang, S. Liu, K. Watanabe, T. Taniguchi, J. Hone, L. Fu, and P. Jarillo-Herrero, Nat. Nanotechnol. 17, 367 (2022).
- [125] Q. Yang, M. Wu, and J. Li, J. Phys. Chem. Lett. 9, 7160 (2018).
- [126] C. R. Woods, P. Ares, H. Nevison-Andrews, M. J. Holwill, R. Fabregas, F. Guinea, A. K. Geim, K. S. Novoselov, N. R. Walet, and L. Fumagalli, Nat. Commun. 12, 347 (2021).
- [127] M. R. Rosenberger, H.-J. Chuang, M. Phillips, V. P. Oleshko, K. M. McCreary, S. V. Sivaram, C. S. Hellberg, and B. T. Jonker, ACS Nano **14**, 4550 (2020).
- [128] D. Zhang, P. Schoenherr, P. Sharma, and J. Seidel, Nat. Rev. Mater. 8, 25 (2023).
- [129] C. N. Lau, M. W. Bockrath, K. F. Mak, and F. Zhang, Nature **602**, 41 (2022).
- [130] R. Bian, R. He, E. Pan, Z. Li, G. Cao, P. Meng, J. Chen, Q. Liu, Z. Zhong, W. Li, and F. Liu, Science (80-.). **385**, 57 (2024).
- [131] K. Yasuda, E. Zalys-Geller, X. Wang, D. Bennett, S. S. Cheema, K. Watanabe, T. Taniguchi, E. Kaxiras, P. Jarillo-Herrero, and R. Ashoori, Science (80-.). **385**, 53 (2024).
- [132] R. Frisenda, E. Navarro-Moratalla, P. Gant, D. Pérez De Lara, P. Jarillo-Herrero, R. V. Gorbachev, and A. Castellanos-Gomez, Chem. Soc. Rev. 47, 53 (2018).

- [133] G. A. Wiegers, Prog. Solid State Chem. **24**, 1 (1996).
- [134] J. Rouxel, Y. Moëlo, A. Lafond, F. J. DiSalvo, A. Meerschaut, and R. Roesky, Inorg. Chem. 33, 3358 (1994).
- [135] N. Ng and T. M. McQueen, APL Mater. 10, (2022).
- [136] R. T. Leriche, A. Palacio-Morales, M. Campetella, C. Tresca, S. Sasaki, C. Brun, F. Debontridder, P. David, I. Arfaoui, O. Šofranko, T. Samuely, G. Kremer, C. Monney, T. Jaouen, L. Cario, M. Calandra, and T. Cren, Adv. Funct. Mater. 31, 1 (2021).
- [137] A. Lafond and A. Meerschaut, Mat. Res. Bull 28, 979 (1993).
- [138] G. R. Reisinger and K. W. Richter, J. Alloys Compd. 891, 161976 (2022).
- [139] S. R. Tamalampudi, J. Y. Lu, N. Rajput, C. Y. Lai, B. Alfakes, R. Sankar, H. Apostoleris, S. P. Patole, I. Almansouri, and M. Chiesa, Npj 2D Mater. Appl. 4, (2020).
- [140] N. Cho, S. Kikkawa, F. Kanamaru, Y. Takeda, O. Yamamoto, H. Kido, and T. Hoshikawa, Solid State Ionics **63–65**, 696 (1993).
- [141] G. R. Reisinger and K. W. Richter, J. Alloys Compd. **881**, 160578 (2021).
- [142] O. L. Sanchez, D. Ovchinnikov, S. Misra, A. Allain, and A. Kis, Nano Lett. **16**, 5792 (2016).
- [143] M. Onoda, K. Kato, Y. Gotoh, and Y. Oosawa, Acta Crystallogr. Sect. B 46, 487 (1990).
- [144] Y. Gotoh, J. Akimoto, and M. Onoda, Mol. Cryst. Liq. Cryst. 341, 885 (2000).
- [145] Y. Ohno, Surf. Sci. 600, 4829 (2006).
- [146] K. Tetalová, Morphology and Physical Properties of Misfit Layer Compound "VPbS3", Charles University, 2022.
- [147] K. Tetalová, Electric Polarization Switching in Moiré Ferroectrics with Electron Beams, Charles University, 2024.
- [148] P. Meng, Y. Wu, R. Bian, E. Pan, B. Dong, X. Zhao, J. Chen, L. Wu, Y. Sun, Q. Fu, Q. Liu, D. Shi, Q. Zhang, Y.-W. Zhang, Z. Liu, and F. Liu, Nat. Commun. 13, 7696 (2022).
- [149] X. Liu, A. P. Pyatakov, and W. Ren, Phys. Rev. Lett. 125, 247601 (2020).
- [150] P. Delavignette and S. Amelinckx, J. Nucl. Mater. 5, 17 (1962).
- [151] K. Ko, A. Yuk, R. Engelke, S. Carr, J. Kim, D. Park, H. Heo, H.-M. Kim, S.-G. Kim, H. Kim, T. Taniguchi, K. Watanabe, H. Park, E. Kaxiras, S. M. Yang, P. Kim, and H. Yoo, Nat. Mater. **22**, 992 (2023).
- [152] I. M. Craig, M. Van Winkle, C. Groschner, K. Zhang, N. Dowlatshahi, Z. Zhu, T. Taniguchi, K. Watanabe, S. M. Griffin, and D. K. Bediako, Nat. Mater. **23**, 323 (2024).
- [153] D. B. Li, D. R. Strachan, J. H. Ferris, and D. A. Bonnell, J. Mater. Res. 21, 935 (2006).
- [154] J. E. Rault, T. O. Mentes, A. Locatelli, and N. Barrett, Sci. Rep. 4, 6792 (2014).
- [155] K. A. Hunnestad, E. D. Roede, A. T. J. Van Helvoort, and D. Meier, J. Appl. Phys. **128**, 191102 (2020).

- [156] F. Sui, H. Li, R. Qi, M. Jin, Z. Lv, M. Wu, X. Liu, Y. Zheng, B. Liu, R. Ge, Y.-N. Wu, R. Huang, F. Yue, J. Chu, and C. Duan, Nat. Commun. **15**, 3799 (2024).
- [157] H. You, Y. Jia, Z. Wu, F. Wang, H. Huang, and Y. Wang, Nat. Comm. 9, 2889 (2018).
- [158] J. Wu, W. Mao, Z. Wu, X. Xu, H. You, A. Xue, and Y. Jia, Nanoscale 8, 7343 (2016).
- [159] L. Xiao, X. Xu, Y. Jia, G. Hu, J. Hu, B. Yuan, Y. Yu, and G. Zou, Nat. Comm. **12**, 318 (2021).
- [160] A. Benke, E. Mehner, M. Rosenkranz, E. Dmitrieva, T. Leisegang, H. Stöcker, W. Pompe, and D. C. Meyer, J. Phys. Chem. C 119, 18278 (2015).
- [161] W. Amdouni, M. Fricaudet, M. Otoničar, V. Garcia, S. Fusil, J. Kreisel, H. Maghraoui-Meherzi, and B. Dkhil, Adv. Mater. **35**, 2301841 (2023).
- [162] L. Jing, Y. Xu, M. Xie, Z. Li, C. Wu, H. Zhao, J. Wang, H. Wang, Y. Yan, N. Zhong, H. Li, and J. Hu, Nano Energy 112, 108508 (2023).
- [163] A. Pálinkás, G. Kálvin, P. Vancsó, K. Kandrai, M. Szendrő, G. Németh, M. Németh, Á. Pekker, J. S. Pap, P. Petrik, K. Kamarás, L. Tapasztó, and P. Nemes-Incze, Nat. Commun. 13, 6770 (2022).
- [164] A. L. Eichhorn, M. Hoffer, and C. Dietz, Carbon N. Y. **200**, 124 (2022).
- [165] L. E. Ştoflea, N. G. Apostol, L. Trupină, and C. M. Teodorescu, J. Mater. Chem. A 2, 14386 (2014).
- [166] E. Emmanouilidou, H. Cao, P. Tang, X. Gui, C. Hu, B. Shen, J. Wu, S.-C. C. Zhang, W. Xie, and N. Ni, Phys. Rev. B **96**, 224405 (2017).
- [167] G. Zanmarchi, J. Phys. Chem. Solids **28**, 2123 (1967).
- [168] D. Mateika, J. Cryst. Growth **13–14**, 698 (1972).
- [169] D. O. Melo, **104**, 780 (1990).
- [170] O. de Melo, F. Leccabue, C. Pelosi, V. Sagredo, M. Chourio, J. Martin, G. Bocelli, and G. Calestani, J. Cryst. Growth **110**, 445 (1991).
- [171] T. Aoyama and K. Ohgushi, Phys. Rev. Mater. **8**, 1 (2024).
- [172] T. Osumi, S. Souma, T. Aoyama, K. Yamauchi, A. Honma, K. Nakayama, T. Takahashi, K. Ohgushi, and T. Sato, Phys. Rev. B **109**, 1 (2024).
- [173] C. Reig, V. Muñoz, C. Gómez, C. Ferrer, and A. Segura, J. Cryst. Growth **223**, 349 (2001).
- [174] Y. GOTOH, M. ONODA, J. AKIMOTO, M. GOTO, and Y. OOSAWA, JAPANESE J. Appl. Phys. PART 1-REGULAR Pap. SHORT NOTES Rev. Pap. **31**, 3946 (1992).
- [175] J. Volný, Microstructures Fabrication for Transport Properties Measurements of Heavy Fermion Compounds, Charles University, 2019.
- [176] P. J. W. Moll, B. Zeng, L. Balicas, S. Galeski, F. F. Balakirev, E. D. Bauer, and F. Ronning, (n.d.).
- [177] F. Balduini, L. Rocchino, A. Molinari, T. Paul, G. Mariani, V. Hasse, C. Felser, C. Zota,

- H. Schmid, and B. Gotsmann, Phys. Rev. Lett. 133, 96601 (2024).
- [178] A. Hunter, C. Putzke, I. Gaponenko, A. Tamai, F. Baumberger, and P. J. W. Moll, Rev. Sci. Instrum. **95**, (2024).
- [179] J. M. De Teresa, Mater. Quantum Technol. 3, (2023).
- [180] K. Höflich, G. Hobler, F. I. Allen, T. Wirtz, G. Rius, L. McElwee-White, A. V. Krasheninnikov, M. Schmidt, I. Utke, N. Klingner, M. Osenberg, R. Córdoba, F. Djurabekova, I. Manke, P. Moll, M. Manoccio, J. M. De Teresa, L. Bischoff, J. Michler, O. De Castro, A. Delobbe, P. Dunne, O. V. Dobrovolskiy, N. Frese, A. Gölzhäuser, P. Mazarov, D. Koelle, W. Möller, F. Pérez-Murano, P. Philipp, F. Vollnhals, and G. Hlawacek, Appl. Phys. Rev. 10, (2023).